

1 **The SC-SNc pathway boosts appetitive locomotion in predatory**
2 **hunting**

3 Meizhu Huang^{1,#}, Dapeng Li^{2,#}, Qing Pei^{2,#}, Zhiyong Xie^{2,#}, Huating Gu^{2,3}, Aixue Liu²,
4 Zijun Chen⁴, Yi Wang⁴, Fangmiao Sun⁵, Yulong Li⁵, Jiayi Zhang⁶, Miao He⁶, Yuan Xie⁷,
5 Fan Zhang⁷, Xiangbing Qi^{2,8}, Congping Shang^{1,*}, Peng Cao^{2,8,*}

6
7 **Affiliation:**

8 ¹Bioland Laboratory (Guangzhou Regenerative Medicine and Health Guangdong
9 Laboratory), 51005 Guangzhou, China

10 ²National Institute of Biological Sciences, Beijing 102206, China

11 ³College of Life Sciences, Beijing Normal University, Beijing 100875, China

12 ⁴State Key Laboratory of Brain and Cognitive Sciences, Institute of Biophysics, Chinese
13 Academy of Sciences, Beijing 100101, China

14 ⁵College of Life Sciences, Peking University, Beijing 100049, China

15 ⁶State Key Laboratory of Medical Neurobiology, Fudan University, 200433 Shanghai,
16 China

17 ⁷Key Laboratory of Neural and Vascular Biology in Ministry of Education, Department of
18 Pharmacology, Hebei Medical University, Shijiazhuang, Hebei, China.

19 ⁸Tsinghua Institute of Multidisciplinary Biomedical Research, Tsinghua University, Beijing
20 100084, China

21

22 # Co-first authors

23

24 * Contact: caopeng@nibs.ac.cn (P.C.) or shangcongping@nibs.ac.cn (C.S.)

25 **ABSTRACT**

26 Appetitive locomotion is essential for organisms to approach rewards, such as food and
27 prey. How the brain controls appetitive locomotion is poorly understood. In a naturalistic
28 goal-directed behavior—predatory hunting, we demonstrate an excitatory brain circuit
29 from the superior colliculus (SC) to the substantia nigra pars compacta (SNc) to boost
30 appetitive locomotion. The SC-SNc pathway transmitted locomotion-speed signals to
31 dopamine neurons and triggered dopamine release in the dorsal striatum. Activation of
32 this pathway increased the speed and frequency of approach during predatory hunting,
33 an effect that depended on the activities of SNc dopamine neurons. Conversely, synaptic
34 inactivation of this pathway impaired appetitive locomotion but not defensive or
35 exploratory locomotion. Together, these data revealed the SC as an important source to
36 provide locomotion-related signals to SNc dopamine neurons to boost appetitive
37 locomotion. (131 words)

38 INTRODUCTION

39 Locomotion plays a fundamental role in the survival of organisms. It can be
40 conceptually divided into three categories: appetitive locomotion, defensive locomotion,
41 and exploratory locomotion (Sinnamon, 1993). These three types of locomotion may be
42 selectively recruited by distinct brain circuits for specific behavioral needs (Ferreira-Pinto
43 et al., 2018). Appetitive locomotion is indispensable for organisms to approach rewarding
44 targets. For example, in a naturalistic goal-directed behavior—predatory hunting,
45 predator employs appetitive locomotion to chase and catch up with prey (Hoy et al., 2016;
46 Han et al., 2017). How the brain control appetitive locomotion during predatory hunting is
47 an unresolved question in the field of neuroethology (Sillar et al., 2016).

48 The superior colliculus (SC) is a multi-layered midbrain structure for sensory
49 information processing and motor functions (Cang et al., 2018; Gandhi and Katnani,
50 2011; Basso and May, 2017). The superficial layers of the SC primarily receive visual
51 inputs (Morin and Studholme, 2014) and perform visual information processing (Wang et
52 al., 2010; De Franceschi and Solomon, 2018). The intermediate and deep layers of the
53 SC are involved in sensorimotor transformation and motor functions (Gandhi and
54 Katnani 2011). The motor functions of the SC include saccadic eye movement (Wurtz
55 and Albano, 1980; Sparks, 1986; Wang et al., 2015), head movement (Isa and Sasaki,
56 2002; Wilson et al., 2018) and locomotion (Cooper et al., 1998; Felsen and Mainen,
57 2008). From a neuroethological perspective, these motor functions of the SC enable
58 itself to orchestrate distinct behavioral actions in predatory hunting in rodents (Furigo et
59 al., 2010; Favaro et al., 2011; Hoy et al., 2019; Shang et al., 2019).

60 How the SC orchestrates distinct behavioral actions during predatory hunting (e.g.
61 approaching and attacking prey) is beginning to be elucidated. With an unbiased
62 activity-dependent genetic labeling approach (FosTRAP2), several hunting-associated
63 tectofugal pathways were identified, such as those projecting to the zona incerta (ZI) and
64 the substantia nigra pars compacta (SNc) (Shang et al., 2019). While the SC-ZI pathway

65 is primarily involved in sensory-triggered predatory attack during hunting, the functional
66 role of the SC-SNc pathway in predatory hunting has not been determined yet.

67 The SC-SNc pathway, also known as tectonigral pathway, was first described by
68 Comoli et al. (2003). It was shown that neurons in the intermediate and deep layers of
69 the SC form synaptic contacts with dopamine and non-dopamine SNc neurons (Comoli
70 et al., 2003). Considering the recent studies showing the involvement of SNc dopamine
71 neurons in the vigor of body movements, including locomotion (Jin and Costa, 2010;
72 Dodson et al., 2016; Howe and Dombeck, 2016; da Silva et al., 2018; Coddington and
73 Dudman, 2018), we hypothesized that the SC-SNc pathway may participate in appetitive
74 locomotion during predatory hunting.

75 In the present study, we explored the role of SC-SNc pathway in appetitive
76 locomotion during predatory hunting. We found that the SC-SNc pathway transmitted
77 locomotion speed signals to SNc dopamine neurons and triggered dopamine release in
78 the dorsal striatum. Activation of this pathway during predatory hunting increased the
79 speed of appetitive locomotion, an effect that depended on the activities of SNc
80 dopamine neurons. Conversely, synaptic inactivation of this pathway impaired appetitive
81 locomotion without changing defensive locomotion. Together, these data revealed the
82 SC as an important source to provide locomotion-related signals to SNc dopamine
83 neurons to boost appetitive locomotion.

84 RESULTS

85 The SC-SNc pathway is primarily glutamatergic

86 We began this study by performing morphological analyses of the SC-SNc pathway.
87 First, we mapped the SC-SNc pathway with cell-type-specific expression of
88 "SynaptoTag" (Xu and Südhof, 2013), which is the enhanced green fluorescent protein
89 fused to synaptic vesicle protein synaptobrevin-2 (EGFP-Syb2). AAV-DIO-EGFP-Syb2
90 was unilaterally injected into the SC of *vGlut2-IRES-Cre* or *GAD2-IRES-Cre* mice (Figure
91 1A and 1C). The specificities of *vGlut2-IRES-Cre* and *GAD2-IRES-Cre* mice to label
92 glutamate+ and GABA+ SC neurons have been validated in an earlier study (Shang et
93 al., 2019). EGFP-Syb2 expression in SC neurons of *vGlut2-IRES-Cre* mice resulted in
94 considerable EGFP-Syb2+ puncta in the SNc (Figure 1B and S1A). In contrast, only
95 sparse EGFP-Syb2+ puncta were observed in the SNc of *GAD2-IRES-Cre* mice (Figure
96 1D and S1B). We normalized the density of EGFP-Syb2 puncta by dividing the puncta
97 density in the SNc with that in the SC of each mouse. Strikingly, the normalized density
98 of EGFP-Syb2 puncta in the SNc of *vGlut2-IRES-Cre* mice was significantly higher than
99 that of *GAD2-IRES-Cre* mice, suggesting that the SC-SNc pathway is primarily
100 glutamatergic (Figure 1E).

101 Second, we retrogradely labeled SNc-projecting SC neurons by injecting CTB-555
102 into the SNc of *WT* mice (Figure 1F). The retrogradely labeled cells (CTB-555+) in the
103 SC were distributed predominantly in the intermediate and deep layers (Figure 1G and
104 S1C). By using primary antibodies that specifically recognize GABA and glutamate
105 (Shang et al., 2018), we found that most of the CTB-555+ cells were
106 immunohistochemically glutamate+ ($92\% \pm 3\%$, $n = 5$ mice; Figure 1H) and GABA-
107 ($91\% \pm 3\%$, $n = 5$ mice; Figure 1I). These data, again, suggested that the SC-SNc
108 pathway is primarily glutamatergic.

109 In addition to the SC-SNc pathway, some SC neurons form another pathway to the
110 ventral tegmental area (VTA) that was implicated in the regulation of sleep and innate
111 defensive responses (Zhang et al., 2019; Zhou et al., 2019). To test whether
112 SNc-projecting SC neurons send collaterals to the VTA, we injected CTB-488 and
113 CTB-555 into the SNc and VTA of the same *WT* mice (Figure S2A). Interestingly, very
114 few cells were dually labeled by CTB-555 and CTB-488 in the SC (Figure S2, B-E). As a
115 negative control, injection of mixed CTB-555 and CTB-488 in the SNc (Figure S2F)
116 resulted in SC neurons co-labeled by both CTB-555 and CTB-488 (Figure S2, G-J).
117 These data suggested that the SC-SNc pathway is anatomically segregated from the
118 SC-VTA pathway.

119 We also examined whether the SNc-projecting SC neurons send collaterals to the ZI,
120 an important center for feeding-related predation (Zhang et al., 2017; Zhao et al., 2019).
121 CTB-488 and CTB-555 were injected into the SNc and ZI of the same mice (Figure S3A).
122 Again, very few cells in the SC were co-labeled by CTB-555 and CTB-488 (Figure S3,
123 B-D), suggesting that the SNc-projecting SC neurons rarely send collaterals to the ZI.

124 **Single SNc-projecting SC neurons encode locomotion speed**

125 To test whether the SC-SNc pathway is involved in locomotion, we made single-unit
126 recording from the SNc-projecting SC neurons by using antidromic activation strategy
127 (Shang et al., 2019). AAV-ChR2-mCherry (Boyden et al., 2005) was injected into the SC
128 of *WT* mice, followed by implantation of an optical fiber above the ChR2-mCherry+ axon
129 terminals in the SNc (Figure S4A). Three weeks after viral injection, single-unit recording
130 was performed with a tungsten electrode in the SC of head-fixed awake mice walking on
131 a cylindrical treadmill (Figure 2A, *left*). The putative SNc-projecting SC neurons were
132 identified by the antidromic action potentials (APs) evoked by light pulses (473 nm, 1 ms,
133 2 mW) that illuminated ChR2-mCherry+ axon terminals in the SNc (Figure 2A, *right*). The
134 antidromically evoked APs had to conform to two criteria (Cohen et al., 2012; Roseberry
135 et al., 2016): First, their waveform should be similar to that of APs during locomotion;

136 second, their latencies to light pulses should be less than 5 ms. With these empirical
137 criteria, we identified 18 units as putative SNc-projecting SC neurons. Their
138 antidromically evoked APs possessed waveforms quantitatively correlated with those of
139 APs during locomotion (Figure S4B and 2B) and had short response latencies to light
140 pulses ($2.7 \text{ ms} \pm 0.4 \text{ ms}$, $n=18$ units; Figure 2C).

141 Then we examined the instantaneous firing rate of these putative SNc-projecting SC
142 neurons before, during and after locomotion on the treadmill. In general, the activities of
143 SNc-projecting SC neurons was modulated by locomotion (Movie S1; Figure 2D). To
144 examine the temporal relationship between the activities of SNc-projecting SC neurons
145 and locomotion initiation, we aligned firing rate of individual units with the onset of
146 locomotion (Figure 2E, *top*). We defined the response onset time as the time when the
147 signal reached 15% of peak amplitude relative to the baseline. The average response
148 curve started to rise at $107 \text{ ms} \pm 15 \text{ ms}$ before locomotion onset ($n = 18$ units; Figure 2E,
149 *bottom*). Similarly, we aligned firing rate of individual units with the offset of locomotion
150 (Figure 2F, *top*), and found that the average response curve dropped to baseline at 121
151 $\text{ms} \pm 16 \text{ ms}$ after locomotion offset ($n = 18$ units; Figure 2F, *bottom*). To examine how the
152 activities of these units were modulated during locomotion, we plotted the
153 response-speed curve of each single-unit (Caggiano et al., 2018) and found a correlation
154 between the firing rate and locomotion speed in the range of $3 \text{ cm/s} \sim 30 \text{ cm/s}$ (Figure
155 2G; Spearman correlation coefficient=0.7528; $P=7.06\text{E-}07$). Histological verification
156 indicated that all the recorded units were localized within the intermediate and deep
157 layers of the SC (Figure 2H and S4C). These data suggested that the SNc-projecting SC
158 neurons encode locomotion speed of mice.

159 **The SC-SNc pathway promotes appetitive locomotion in predatory hunting**

160 To further explore the role of SC-SNc pathway in locomotion, we examined whether
161 activation of this pathway promotes locomotion. AAV-ChR2-mCherry was bilaterally
162 injected into the SC of *WT* mice (Figure 3A and S5A), followed by implantation of an

163 optical fiber above the ChR2-mCherry+ axon terminals in the SNc (Figure 3B). In acute
164 brain slices with the SC, light pulses (10 Hz, 2 ms, 10 mW) reliably evoked action
165 potentials from ChR2-mCherry+ SC neurons (Figure S5B). In a linear runway (Figure
166 3C), photostimulation of the SC-SNc pathway (10 Hz, 20 ms, 6 s, 10 mW) increased
167 locomotion speed of mice (Figure 3D and 3E). In control mice injected with AAV-mCherry
168 in the SC, light illumination on mCherry+ axon terminals in the SNc did not promote
169 locomotion speed (Figure 3D and 3E). In addition, we found that the effects of SC-SNc
170 pathway activation on locomotion speed depended on the frequency of light stimulation
171 (Figure S5C).

172 Then we tested whether activation of the SC-SNc pathway boosts appetitive
173 locomotion during predatory hunting. In predatory hunting, appetitive locomotion
174 occurred when predator approached prey (Figure 3F). By measuring the instantaneous
175 azimuth angle and distance between prey and predator (Figure S5D), we were able to
176 identify a series of intermittent approach episodes (Figure S5E) according to the
177 established criteria (Hoy et al., 2016). Appetitive locomotion in these approach episodes
178 was quantitatively assessed by measuring the speed of approach and frequency of
179 approach. The speed of approach was calculated by averaging the peak speed of each
180 approach episode in the trial. The frequency of approach was the number of approach
181 episodes divided by total time of the trial. With the method above, we labeled the
182 approach episodes (shaded areas in orange) in the behavioral ethogram of predatory
183 hunting in mice without (OFF) and with (ON) photostimulation of the SC-SNc pathway
184 (10 Hz, 20 ms, 10 mW) (Movie S2 and S3; Figure 3G and 3H). We found that activation
185 of the SC-SNc pathway significantly increased the speed of approach (Figure 3I),
186 increased the frequency of approach (Figure 3J) and reduced the time required for prey
187 capture (Figure 3K). In contrast, the latency and the frequency of predatory attack with
188 jaw during hunting were not altered by activation of the SC-SNc pathway (Figure 3, L and

189 M). These data suggested that activation of the SC-SNc pathway specifically promoted
190 appetitive locomotion during predatory hunting.

191 **The SC-SNc pathway is required for appetitive locomotion in predatory hunting**

192 Then we examined whether the SC-SNc pathway is required for appetitive
193 locomotion during predatory hunting, by synaptically inactivating the SNc-projecting SC
194 neurons. Tetanus neurotoxin (TeNT), which blocks neurotransmitter release by
195 proteolytic cleavage of synaptobrevin-2 (Schiavo et al., 1992), has been used as a
196 molecular tool for synaptic inactivation (Xu and Südhof, 2013; Cregg et al., 2020). The
197 effectiveness and specificity of TeNT-mediated synaptic inactivation of SC neurons have
198 been validated in a previous study (Shang et al., 2019). To synaptically inactivate the
199 SC-SNc pathway, we injected AAV2-retro-mCherry-IRES-Cre (Tervo et al, 2016) and
200 AAV-DIO-EGFP-2A-TeNT into the SNc and SC of *WT* mice, respectively (Figure 4A).
201 The injection of AAV2-retro-mCherry-IRES-Cre in the SNc (Figure S6A) and
202 AAV-DIO-EGFP-2A-TeNT in the SC cooperatively labeled SNc-projecting SC neurons
203 with EGFP (Figure 4B, *top*), as demonstrated by the co-expression of mCherry and
204 EGFP in the same SC neurons (Figure 4B, *bottom*).

205 Then we analyzed the effects of SC-SNc pathway inactivation on predatory hunting
206 behavior in mice. We labeled the approach episodes (shaded areas in orange) in the
207 behavioral ethogram of predatory hunting in mice without (Ctrl) and with (TeNT) synaptic
208 inactivation of the SC-SNc pathway (Movie S4 and S5; Figure 4C and 4D).
209 TeNT-mediated inactivation of SC-SNc pathway impaired predatory hunting by
210 significantly increasing the time required for prey capture (Figure 4E). Such effect on
211 hunting could not be explained by an impairment of predatory attack, because neither
212 the latency nor the frequency of jaw attack during hunting was changed by SC-SNc
213 pathway inactivation (Figure 4F and 4G). In contrast, both the speed of approach and
214 frequency of approach in predatory hunting were significantly decreased (Figure 4H and

215 4l). These data suggested that the SC-SNc pathway is required for appetitive locomotion
216 during predatory hunting.

217 We also tested the role of the SC-SNc pathway in defensive and exploratory
218 locomotion. In response to looming visual stimuli, mice exhibited escape behavior to
219 avoid the imminent threats (Yilmaz and Meister, 2013). The escape behavior was used to
220 measure defensive locomotion (Caggiano et al., 2018). We found that mice without (Ctrl)
221 and with (TeNT) synaptic inactivation of the SC-SNc pathway exhibited escape followed
222 by freezing in response to looming visual stimuli (Movie S6 and S7; Figure S6D and
223 S6E). Quantitative analyses of locomotion speed indicated that synaptic inactivation of
224 the SC-SNc pathway did not alter the peak speed of escape behavior during looming
225 visual stimuli (Figure S6F) or average speed after stimuli (Figure S6G), suggesting this
226 pathway is not required for defensive locomotion. Moreover, these mice exhibited similar
227 average locomotion speed before looming visual stimuli (Figure S6H), suggesting that
228 the SC-SNc pathway may not be involved in exploratory locomotion as well.

229 **The SC-SNc pathway preferentially innervates SNc dopamine neurons**

230 To explore how the SC-SNc pathway is synaptically connected to the SNc, we
231 employed mouse lines to genetically label different neuronal subtypes in the SNc. The
232 most prominent neuronal subtype in the SNc is the dopamine neurons positive for
233 tyrosine hydroxylase (TH⁺). These SNc dopamine neurons are largely segregated from
234 those expressing glutamate decarboxylase-2 (GAD2⁺) (Tritsch et al., 2014; Kim et al.,
235 2015) or vesicular glutamate transporter-2 (vGlut2⁺) (Kawano et al., 2006; Morales and
236 Root, 2014). Although *TH-GFP* mice (Sawamoto et al., 2001) did not reliably label
237 dopamine neurons in the VTA, this line marked SNc dopamine neurons with higher
238 fidelity (Lammel et al., 2015). We confirmed this observation (Figure S7A and S7B) and
239 used *TH-GFP* mice to genetically label SNc dopamine neurons in this study. By crossing
240 *Ai14* (Madisen et al., 2010) with *GAD2-IRES-Cre* mice (Taniguchi et al., 2011), we
241 labeled putative SNc GAD2⁺ neurons with tdTomato (GAD2-tdT; Figure S7C and S7D).

242 Similarly, *Ai14* was crossed with *vGlut2-IRES-Cre* mice (Vong et al., 2011) to label
243 putative SNc vGlut2+ neurons with tdTomato (vGlut2-tdT; Figure S7E and S7F).

244 To examine how the SC-SNc pathway synaptically innervates SNc dopamine
245 neurons and GAD2+ neurons, we generated *GAD2-IRES-Cre/Ai14/TH-GFP* triple
246 transgenic mice. In this mouse line, putative SNc dopamine neurons were genetically
247 labeled by GFP (TH-GFP+), whereas putative GAD2+ neurons were identified as those
248 positive for tdTomato (GAD2-tdT+) (Figure 5A). AAV-ChR2-mCherry was injected into
249 the SC of *GAD2-IRES-Cre/Ai14/TH-GFP* mice (Figure 5C, *left*). In acute brain slice with
250 the SNc, we illuminated ChR2-mCherry+ axon terminals with light-pulses (473 nm, 2 ms)
251 with saturating power (20 mW), while performing whole-cell recordings from TH-GFP+
252 and adjacent GAD2-tdT+ neurons (Figure 5C, *right*). Using low-chloride internal solution
253 (Kim et al., 2015), we recorded optogenetically-evoked excitatory postsynaptic currents
254 (oEPSCs, voltage clamp at -70 mV) and inhibitory postsynaptic currents (oIPSCs,
255 voltage clamp at 0 mV), which were removed by perfusion of antagonists of glutamate
256 receptors (APV & CNQX) and GABA_A receptor (picrotoxin), respectively (Figure S7, G-I).
257 We found that the amplitude of oEPSCs was significantly higher than that of oIPSCs in
258 both SNc GAD2-tdT+ and TH-GFP+ neurons (Figure 5, D and E). This was consistent
259 with the morphological observation that the SNc-projecting SC neurons are primarily
260 glutamatergic (Figure 1). Moreover, the amplitude of oEPSCs in TH-GFP+ neurons was
261 significantly higher than that in GAD2-tdT+ neurons (Figure 5, D and E), suggesting that
262 the SC-SNc pathway preferentially innervate SNc dopamine neurons.

263 To test how the SC-SNc pathway is synaptically connected to SNc vGlut2+ neurons,
264 we generated *vGlut2-IRES-Cre/Ai14/TH-GFP* triple transgenic mice. In this mouse line,
265 putative SNc dopamine neurons were genetically labeled by GFP (TH-GFP+), whereas
266 putative vGlut2+ neurons were identified as those positive for tdTomato (vGlut2-tdT+)
267 (Figure 5B). We injected AAV-ChR2-mCherry into the SC of triple transgenic mice
268 (Figure 5C, *left*). In acute brain slices with the SNc, we recorded oEPSCs and oIPSCs

269 from TH-GFP+ and adjacent vGlut2-tdT+ neurons (Figure 5C, *right*). We found that the
270 amplitude of oEPSCs was significantly higher than that of oIPSCs in both TH-GFP+ and
271 vGlut2-tdT+ neurons (Figure 5, F and G). Moreover, the amplitude of oEPSCs in
272 TH-GFP+ neurons was significantly higher than that in vGlut2-tdT+ neurons (Figure 5, F
273 and G). These data indicated that the SC-SNc pathway has a stronger synaptic
274 connection with SNc dopamine neurons than their synaptic connections to GAD2+ or
275 vGlut2+ non-dopamine neurons.

276 **Activation of the SC-SNc pathway triggers striatal dopamine release**

277 To further confirm that the SNc dopamine neurons are the postsynaptic target of
278 SC-SNc pathway, we examined whether activation of this pathway evoke dopamine
279 release in the dorsal striatum (Lerner et al., 2015). To monitor dopamine release, we
280 employed genetically encoded GPCR-activation-based dopamine sensor (GRAB_{DA}
281 sensor) that reports dopamine dynamics of nigrostriatal pathway (Sun et al., 2018).
282 AAV-C1V1-mCherry (Yizhar et al., 2011) and AAV-GRAB_{DA} were injected into the SC and
283 dorsal striatum of *WT* mice (Figure 6A), followed by implantation of optical fibers above
284 the SNc and dorsal striatum, respectively (Figure 6B). The viral expression and optical
285 fiber implantation were validated by using immunohistochemistry and slice physiology
286 (Figure 6, C-F).

287 Then we tested whether activation of the SC-SNc pathway triggers dopamine
288 release in the dorsal striatum. In freely moving mice, single light-pulses (561nm, 2 ms,
289 0~20 mW) stimulating the axon terminals of SNc-projecting SC neurons (Figure 6, B and
290 E) transiently increased the fluorescence of GRAB_{DA} sensor in the dorsal striatum
291 (Figure 6, G and H). As a control, no obvious fluorescence changes were observed in
292 striatal neurons expressing EGFP (Figure 6, G and H). Moreover, the light-evoked
293 GRAB_{DA} signals were abrogated by D2 receptor antagonist haloperidol (Figure 6, I and
294 J). These data indicated that SC-SNc pathway activation triggers dopamine release in

295 the dorsal striatum, supporting that the SNc dopamine neurons are the postsynaptic
296 target of the SC-SNc pathway.

297 **SNc dopamine neurons mediate appetitive locomotion evoked by SC-SNc pathway**

298 Then we asked whether the SNc dopamine neurons mediate appetitive locomotion
299 evoked by SC-SNc pathway. To address this question, we employed the strategy of
300 designer receptors exclusively activated by designer drugs (DREADD) to
301 chemogenetically silence SNc dopamine neurons (Armbruster et al., 2007).
302 AAV-DIO-hM4Di-mCherry and AAV-ChR2-EYFP were injected into the SNc and SC of
303 *DAT-IRES-Cre* mice (Backman et al., 2006) bilaterally, followed by two optical fibers
304 implanted above the SNc (Figure 7, A and B). AAV-DIO-mCherry was used as a control
305 of AAV-DIO-hM4Di-mCherry. In the SC, the expression of ChR2-EYFP and the efficiency
306 to evoke action potentials from ChR2-EYFP+ neurons were validated (Figure S8A and
307 S8B). In the ventral midbrain, hM4Di-mCherry was specifically expressed in SNc
308 dopamine neurons that were intermingled with ChR2-EYFP+ axon terminals from SC
309 neurons (Figure 7C). Chemogenetic suppression of neuronal firing by Clozapine N-oxide
310 (CNO, 10 μ M) was confirmed in slice physiology (Figure 7D).

311 To test whether SNc dopamine neurons mediate the appetitive locomotion evoked by
312 SC-SNc pathway activation, we intraperitoneally treated the mice with saline or CNO.
313 Light stimulation of SC-SNc pathway of mice treated with saline significantly increased
314 the speed of approach (Figure 7E, *left*) and the frequency of approach (Figure 7G, *left*)
315 during predatory hunting. When the same mice were treated with CNO (1 mg/kg) to
316 chemogenetically suppress the activities of SNc dopamine neurons, activation of
317 SC-SNc pathway only mildly increased the speed of approach (Figure 7E, *right*) and the
318 frequency of approach (Figure 7G, *right*). For each mouse, we calculated “net increase”
319 of approach speed by subtracting speed of approach during laser OFF from that during
320 laser ON. It turned out that chemogenetic inactivation of SNc dopamine neurons with
321 CNO prevented the net increase of approach speed (Figure 7F). Similarly, we calculated

322 “net increase” of approach frequency by subtracting frequency of approach during laser
323 OFF from that during laser ON. We found that inactivation of SNc dopamine neurons
324 prevented the net increase of approach frequency during predatory hunting (Figure 7H).
325 These data suggested that the activities of SNc dopamine neurons are required for the
326 appetitive locomotion evoked by SC-SNc pathway.

327 **DISCUSSION**

328 Appetitive locomotion is required for organisms to approach incentive stimuli in
329 goal-directed behaviors. How the brain controls appetitive locomotion is poorly
330 understood. Here we used predatory hunting as a behavior paradigm to address this
331 question. We demonstrate an excitatory subcortical circuit from the SC to the SNc to
332 boost appetitive locomotion. The SC-SNc pathway transmits locomotion-speed signals
333 to dopamine neurons and triggers dopamine release in the dorsal striatum. Activation of
334 this pathway promoted appetitive locomotion during predatory hunting, whereas synaptic
335 inactivation of this pathway impairs appetitive locomotion rather than defensive
336 locomotion. Together, these data reveal the SC as an important source to provide
337 locomotion-related signals to SNc dopamine neurons to boost appetitive locomotion.

338 **The brain circuits for predatory hunting: the SC and beyond**

339 As a naturalistic goal-directed behavior, predatory hunting has been the focus of
340 studies using diverse animal models, such as toad (Ewert, 1997), zebrafish (Gahtan et
341 al., 2005; Bianco et al., 2011; Trivedi and Bollmann, 2013) and rodents (Anjum et al.,
342 2006; Hoy et al., 2016). In these animal models, it was found that the optic tectum (OT)
343 and its mammalian homolog, the SC, play a fundamental role in predatory hunting (Toad:
344 Ewert, 1997; Zebrafish: Del Bene et al., 2010; Bianco and Engert, 2015; Rodents: Furigo
345 et al., 2010; Favaro et al., 2011). In rodents, a recent study has shown that
346 genetically-defined neuronal subtypes in the SC make distinct contributions to prey
347 capture behavior in mice (Hoy et al., 2019). The hunting-associated SC neurons may
348 form divergent neural pathways to orchestrate distinct behavioral actions during
349 predatory hunting, such as attacking prey (Shang et al., 2019) and, as demonstrated in
350 this study, appetitive locomotion for approaching prey.

351 In another line of research, it was found that brain areas, which were thought to be
352 related to food intake, are also involved in predatory hunting. For example, optogenetic

353 activation of GABAergic neurons in the central amygdala (CeA), the lateral
354 hypothalamus (LH), or the ZI provoked strong predatory hunting in mice (Han et al., 2017;
355 Li et al., 2018; Zhao et al., 2019). The involvement of feeding-related areas in predatory
356 hunting may be evolutionarily conserved, because the inferior lobe of hypothalamus in
357 zebrafish also participates in prey capture behavior (Muto et al., 2017). In addition,
358 activation of CaMKII α -positive neurons in the medial preoptic area (MPA), which is
359 related to object craving, also induces hunting-like actions toward prey (Park et al., 2018).
360 Understanding how the neurons in the SC and in these newly-discovered brain areas
361 coordinately control predatory hunting is a challenging task for future study.

362 **Dopamine system modulates predatory hunting**

363 As an important neuromodulatory system in the brain, dopamine system plays a
364 critical role in conditioned and unconditioned appetitive behaviors (Schultz, 2007;
365 Bromberg-Martin et al., 2010). Earlier studies using systemic treatment of agonists or
366 antagonists of dopamine receptors have demonstrated strong effects of dopaminergic
367 modulation on predatory hunting in mammals (Schmidt, 1983; Shaikh et al., 1991; Tinsley
368 et al., 2000). However, two critical questions remained unanswered. First, how is
369 dopamine system recruited during predatory hunting? Second, considering the multiple
370 clusters of dopamine neurons in the brain, which specific clusters of dopamine neurons
371 participate in modulating predatory hunting? In this study, we show that the dopamine
372 neurons in the SNc are innervated by the SC, a central hub to orchestrate predatory
373 hunting. The SC-SNc pathway may provide locomotion-related signals to SNc dopamine
374 neurons to boost appetitive locomotion during predatory hunting. These results may
375 provide some clues to the above unanswered questions. They supported the recent
376 studies showing the involvement of SNc dopamine neurons in the vigor of body
377 movements (Jin and Costa, 2010; Dodson et al., 2016; Howe and Dombeck, 2016; da
378 Silva et al., 2018; Coddington and Dudman, 2018).

379 **More considerations on the functions of SC-SNc pathway**

380 In their seminal studies, Redgrave and colleagues proposed that the SC-SNc
381 pathway may serve as a route for salient visual stimuli to drive phasic activities of
382 dopamine neurons (Dommett et al., 2005). In primate, this pathway may mediate
383 visually-evoked reward expectation signals in dopamine neurons during reinforcement
384 learning (Takakuwa et al., 2017). In the present study, we recorded single-unit activity of
385 SNc-projecting SC neurons in head-fixed walking mice (Movie S1), and unexpectedly
386 found that the SNc-projecting SC neurons encode locomotion speed (Figure 2). This
387 observation prompted us to examine the role of the SC-SNc pathway in regulating
388 locomotion during predatory hunting (Figure 3-7). Our data may have added another
389 perspective for understanding the functions of the SC-SNc pathway. Although we did not
390 systematically examine the sensory responses of the recorded neurons, we do not rule
391 out the possibility that these neurons may respond to salient sensory stimuli (e.g. visual
392 or vibrissal tactile stimuli). In future study, it will be interesting to explore whether the
393 SC-SNc pathway can integrate both sensory and locomotion-related signals to
394 dynamically modulate appetitive locomotion during hunting.

395 **The origin of locomotion-related signals of SNc-projecting SC neurons**

396 Where do the locomotion-speed signals of the SNc-projecting SC neurons originate?
397 Several motor-related brain areas (e.g. SNr, PPTg, and motor cortex) directly project to
398 the SC and may provide motor signals to the SC (Comoli et al., 2012). This speculation
399 was supported by a recent study showing that the projection from the SNr is the
400 strongest among the above motor-related brain areas (Doykos et al., 2020). The axons
401 of GABAergic SNr neurons terminate in the lateral part of deep layers of the SC (Kaneda
402 et al., 2008), a region that contains SNc-projecting SC neurons studied here. The
403 inhibition and excitation of SNr neurons well predict the initiation and suppression of
404 locomotion, respectively (Freeze et al., 2013). These studies suggested that
405 locomotion-related signals of SNc-projecting SC neurons may at least partially originate
406 from the SNr, which is the primary output of basal ganglia.

407 **SUPPLEMENTARY INFORMATION**

408 Supplementary information includes eight figures, seven movies and four tables.

409

410 **ACKNOWLEDGMENTS**

411 We thank Drs. Thomas Südhof, Karl Deisseroth and Minmin Luo for providing plasmids
412 and mouse lines. This work was supported by the National Natural Science Foundation
413 of China (31925019 and 31671095 to P.C., 31771150 to Y.W., Top talent program of
414 Hebei province to F.Z.), the open funds of the State Key Laboratory of Medical
415 Neurobiology, and the Institutional Funding from NIBS. All data are archived in NIBS.

416

417 **AUTHOR CONTRIBUTIONS**

418 P.C., C.S., J.Z., M.H., and F.Z. conceived the study. C.S., M.H., Q.P., and A.L. did
419 injections and fiber implantation. C.S., Z.X., Q.P., H.G., and Y.X. did behavioral tests.
420 C.S. did single-unit recording. M.H. did histological analyses. C.S. and Z.C. did slice
421 physiology. Y.W., F.S., Y.L., J.Z., F.Z., M.H., and X.Q. provided reagents. D.L., C.S.,
422 Z.X., H.G., Z.C. and P.C. analyzed data. P.C. wrote the manuscript.

423

424 **DECLARATION OF INTERESTS**

425 The authors declare no competing financial interests.

426 **REFERENCES**

- 427 1. Anjum F, Turni H, Mulder PG, van der Burg J, Brecht M. Tactile guidance of prey
428 capture in Etruscan shrews. *PNAS* 103, 16544-16549 (2006).
- 429 2. Armbruster BN, Li X, Pausch MH, Herlitze S, Roth BL. Evolving the lock to fit the key
430 to create a family of G protein-coupled receptors potently activated by an inert ligand.
431 *PNAS* 104, 5163-5168 (2007).
- 432 3. Backman CM, et al. Characterization of a mouse strain expressing Cre recombinase
433 from the 3' untranslated region of the dopamine transporter locus. *Genesis* 44,
434 383-390 (2006).
- 435 4. Basso MA, May PJ. Circuits for Action and Cognition: A View from the Superior
436 Colliculus. *Annu Rev Vis Sci* 3, 197-226 (2017).
- 437 5. Bianco IH, Engert F. Visuomotor transformations underlying hunting behavior in
438 zebrafish. *Current Biology* 25, 831-846 (2015).
- 439 6. Bianco IH, Kampff AR, Engert F. Prey capture behavior evoked by simple visual
440 stimuli in larval zebrafish. *Frontiers in Systems Neurosci.* 5, 101 (2011).
- 441 7. Boyden ES, Zhang F, Bamberg E, Nagel G, Deisseroth K. Millisecond-timescale,
442 genetically targeted optical control of neural activity. *Nature Neuroscience* 8,
443 1263-1268 (2005).
- 444 8. Bromberg-Martin ES, Matsumoto M, Hikosaka O. Dopamine in motivational control:
445 rewarding, aversive, and alerting. *Neuron* 68, 815-834 (2010).
- 446 9. Caggiano V, et al. Midbrain circuits that set locomotor speed and gait selection.
447 *Nature* 553, 455-460 (2018).
- 448 10. Cang J, Savier E, Barchini J, Liu X. Visual Function, Organization, and Development
449 of the Mouse Superior Colliculus. *Annu Rev Vis Sci* 4, 239-262 (2018).
- 450 11. Coddington LT, Dudman JT. The timing of action determines reward prediction
451 signals in identified midbrain dopamine neurons. *Nature Neurosci.* 21, 1563-1573
452 (2018).
- 453 12. Cohen JY, Haesler S, Vong L, Lowell BB, Uchida N. Neuron-type-specific signals for
454 reward and punishment in the ventral tegmental area. *Nature* 482, 85-88 (2012).
- 455 13. Comoli E, et al. A direct projection from superior colliculus to substantia nigra for
456 detecting salient visual events. *Nature Neuroscience* 6, 974-980 (2003).
- 457 14. Comoli E, Das Neves Favaro P, Vautrelle N, Leriche M, Overton PG, Redgrave P.
458 Segregated anatomical input to sub-regions of the rodent superior colliculus
459 associated with approach and defense. *Front Neuroanat* 6, 9 (2012).
- 460 15. Cooper BG, Miya DY, Mizumori SJ. Superior colliculus and active navigation: role of

- 461 visual and non-visual cues in controlling cellular representations of space.
462 Hippocampus 8, 340-372 (1998).
- 463 16. Cregg JM, Leiras R, Montalant A, Wanken P, Wickersham IR, Kiehn O. Brainstem
464 neurons that command mammalian locomotor asymmetries. *Nature Neurosci.* 23,
465 730-740 (2020).
- 466 17. da Silva JA, Tecuapetla F, Paixao V, Costa RM. Dopamine neuron activity before
467 action initiation gates and invigorates future movements. *Nature* 554, 244-248
468 (2018).
- 469 18. De Franceschi G, Solomon SG. Visual response properties of neurons in the
470 superficial layers of the superior colliculus of awake mouse. *The Journal of*
471 *physiology* 596, 6307-6332 (2018).
- 472 19. Del Bene F, et al. Filtering of visual information in the tectum by an identified neural
473 circuit. *Science* 330, 669-673 (2010).
- 474 20. Dodson PD, et al. Representation of spontaneous movement by dopaminergic
475 neurons is cell-type selective and disrupted in parkinsonism. *PNAS* 113, E2180-2188
476 (2016).
- 477 21. Dommett E, et al. How visual stimuli activate dopaminergic neurons at short latency.
478 *Science* 307, 1476-1479 (2005).
- 479 22. Doykos TK, Gilmer JI, Person AL, Felsen G. Monosynaptic inputs to specific cell
480 types of the intermediate and deep layers of the superior colliculus. *The Journal of*
481 *comparative neurology* 528, 2254-2268 (2020).
- 482 23. Ewert JP. Neural correlates of key stimulus and releasing mechanism: a case study
483 and two concepts. *Trends in Neurosci.* 20(8):332-339 (1997)
- 484 24. Favaro PD, Gouvea TS, de Oliveira SR, Vautrelle N, Redgrave P, Comoli E. The
485 influence of vibrissal somatosensory processing in rat superior colliculus on prey
486 capture. *Neuroscience* 176, 318-327 (2011).
- 487 25. Felsen G, Mainen ZF. Neural substrates of sensory-guided locomotor decisions in
488 the rat superior colliculus. *Neuron* 60, 137-148 (2008).
- 489 26. Ferreira-Pinto MJ, Ruder L, Capelli P, Arber S. Connecting Circuits for Supraspinal
490 Control of Locomotion. *Neuron* 100, 361-374 (2018).
- 491 27. Freeze BS, Kravitz AV, Hammack N, Berke JD, Kreitzer AC. Control of basal ganglia
492 output by direct and indirect pathway projection neurons. *The Journal of*
493 *Neuroscience* 33, 18531-18539 (2013).
- 494 28. Furigo IC, et al. The role of the superior colliculus in predatory hunting. *Neuroscience*
495 165, 1-15 (2010).
- 496 29. Gahtan E, Tanger P, Baier H. Visual prey capture in larval zebrafish is controlled by

- 497 identified reticulospinal neurons downstream of the tectum. *The Journal of*
498 *neuroscience* 25, 9294-9303 (2005).
- 499 30. Gandhi NJ, Katnani HA. Motor functions of the superior colliculus. *Annu Rev*
500 *Neurosci* 34, 205-231 (2011).
- 501 31. Han W, et al. Integrated Control of Predatory Hunting by the Central Nucleus of the
502 Amygdala. *Cell* 168, 311-324 e318 (2017).
- 503 32. Howe MW, Dombeck DA. Rapid signalling in distinct dopaminergic axons during
504 locomotion and reward. *Nature* 535, 505-510 (2016).
- 505 33. Hoy JL, Bishop HI, Niell CM. Defined cell types in superior colliculus make distinct
506 contributions to prey capture behavior in the mouse. *Current Biology* 29, 4130-4138
507 e4135 (2019).
- 508 34. Hoy JL, Yavorska I, Wehr M, Niell CM. Vision Drives Accurate Approach Behavior
509 during Prey Capture in Laboratory Mice. *Current Biology* 26, 3046-3052 (2016).
- 510 35. Isa T, Sasaki S. Brainstem control of head movements during orienting; organization
511 of the premotor circuits. *Progress in Neurobiology* 66, 205-241 (2002).
- 512 36. Jin X, Costa RM. Start/stop signals emerge in nigrostriatal circuits during sequence
513 learning. *Nature* 466, 457-462 (2010).
- 514 37. Kaneda K, Isa K, Yanagawa Y, Isa T. Nigral inhibition of GABAergic neurons in
515 mouse superior colliculus. *The Journal of Neuroscience* 28, 11071-11078 (2008).
- 516 38. Kawano M, et al. Particular subpopulations of midbrain and hypothalamic dopamine
517 neurons express vesicular glutamate transporter 2 in the rat brain. *The Journal of*
518 *comparative neurology* 498, 581-592 (2006).
- 519 39. Kim JI, et al. Aldehyde dehydrogenase 1a1 mediates a GABA synthesis pathway in
520 midbrain dopaminergic neurons. *Science* 350, 102-106 (2015).
- 521 40. Lammel S, et al. Diversity of transgenic mouse models for selective targeting of
522 midbrain dopamine neurons. *Neuron* 85, 429-438 (2015).
- 523 41. Lerner TN, et al. Intact-Brain Analyses Reveal Distinct Information Carried by SNc
524 Dopamine Subcircuits. *Cell* 162, 635-647 (2015).
- 525 42. Li Y, et al. Hypothalamic Circuits for Predation and Evasion. *Neuron* 97, 911-924
526 e915 (2018).
- 527 43. Madisen L, et al. A robust and high-throughput Cre reporting and characterization
528 system for the whole mouse brain. *Nature Neuroscience* 13, 133-140 (2010).
- 529 44. Morales M, Root DH. Glutamate neurons within the midbrain dopamine regions.
530 *Neuroscience* 282, 60-68 (2014).
- 531 45. Morin LP, Studholme KM. Retinofugal projections in the mouse. *The Journal of*

- 532 comparative neurology 522, 3733-3753 (2014).
- 533 46. Muto A, Lal P, Ailani D, Abe G, Itoh M, Kawakami K. Activation of the hypothalamic
534 feeding centre upon visual prey detection. *Nature communications* 8, 15029 (2017).
- 535 47. Park SG, et al. Medial preoptic circuit induces hunting-like actions to target objects
536 and prey. *Nature neuroscience* 21, 364-372 (2018).
- 537 48. Roseberry TK, Lee AM, Lalive AL, Wilbrecht L, Bonci A, Kreitzer AC.
538 Cell-Type-Specific Control of Brainstem Locomotor Circuits by Basal Ganglia. *Cell*
539 164, 526-537 (2016).
- 540 49. Sawamoto K, et al. Visualization, direct isolation, and transplantation of midbrain
541 dopaminergic neurons. *PNAS* 98, 6423-6428 (2001).
- 542 50. Schiavo G, et al. Tetanus and botulinum-B neurotoxins block neurotransmitter
543 release by proteolytic cleavage of synaptobrevin. *Nature* 359, 832-835 (1992).
- 544 51. Schmidt WJ. Involvement of dopaminergic neurotransmission in the control of
545 goal-directed movements. *Psychopharmacology* 80, 360-364 (1983).
- 546 52. Schultz W. Multiple dopamine functions at different time courses. *Annu Rev Neurosci*
547 30, 259-288 (2007).
- 548 53. Shaikh MB, Lu CL, MacGregor M, Siegel A. Dopaminergic regulation of quiet biting
549 attack behavior in the cat. *Brain research bulletin* 27, 725-730 (1991).
- 550 54. Shang C, et al. A subcortical excitatory circuit for sensory-triggered predatory hunting
551 in mice. *Nature neuroscience* 22, 909-920 (2019).
- 552 55. Sillar K, Picton L, Heitler W. *The neuroethology of predation and escape.*
553 Wiley-Blackwell (2016).
- 554 56. Sinnamon HM. Preoptic and hypothalamic neurons and the initiation of locomotion in
555 the anesthetized rat. *Progress in neurobiology* 41, 323-344 (1993).
- 556 57. Sparks DL. Translation of sensory signals into commands for control of saccadic eye
557 movements: role of primate superior colliculus. *Physiol Rev* 66, 118-171 (1986).
- 558 58. Sun F, et al. A Genetically Encoded Fluorescent Sensor Enables Rapid and Specific
559 Detection of Dopamine in Flies, Fish, and Mice. *Cell* 174, 481-496 e419 (2018).
- 560 59. Takakuwa N, Kato R, Redgrave P, Isa T. Emergence of visually-evoked reward
561 expectation signals in dopamine neurons via the superior colliculus in V1 lesioned
562 monkeys. *Elife* 6, (2017).
- 563 60. Taniguchi H, et al. A resource of Cre driver lines for genetic targeting of GABAergic
564 neurons in cerebral cortex. *Neuron* 71, 995-1013 (2011).
- 565 61. Tervo DG, et al. A Designer AAV Variant Permits Efficient Retrograde Access to
566 Projection Neurons. *Neuron* 92, 372-382 (2016).

- 567 62. Tinsley MR, Rebec GV, Timberlake W. Facilitation of preparatory behavior in an
568 artificial prey paradigm by D1-subfamily dopamine receptor activation. *Behavioural*
569 *brain research* 114, 23-30 (2000).
- 570 63. Tritsch NX, Oh WJ, Gu C, Sabatini BL. Midbrain dopamine neurons sustain inhibitory
571 transmission using plasma membrane uptake of GABA, not synthesis. *Elife* 3,
572 e01936 (2014).
- 573 64. Trivedi CA, Bollmann JH. Visually driven chaining of elementary swim patterns into a
574 goal-directed motor sequence: a virtual reality study of zebrafish prey capture.
575 *Frontiers in neural circuits* 7, 86 (2013).
- 576 65. Vong L, Ye C, Yang Z, Choi B, Chua S, Jr., Lowell BB. Leptin action on GABAergic
577 neurons prevents obesity and reduces inhibitory tone to POMC neurons. *Neuron* 71,
578 142-154 (2011).
- 579 66. Wang L, Liu M, Segraves MA, Cang J. Visual Experience Is Required for the
580 Development of Eye Movement Maps in the Mouse Superior Colliculus. *The Journal*
581 *of Neuroscience* 35, 12281-12286 (2015).
- 582 67. Wang L, Sarnaik R, Rangarajan K, Liu X, Cang J. Visual receptive field properties of
583 neurons in the superficial superior colliculus of the mouse. *The Journal of*
584 *Neuroscience* 30, 16573-16584 (2010).
- 585 68. Wilson JJ, Alexandre N, Trentin C, Tripodi M. Three-Dimensional Representation of
586 Motor Space in the Mouse Superior Colliculus. *Current Biology* 28, 1744-1755 e1712
587 (2018).
- 588 69. Wurtz RH, Albano JE. Visual-motor function of the primate superior colliculus. *Annu*
589 *Rev Neurosci* 3, 189-226 (1980).
- 590 70. Xu W, Sudhof TC. A neural circuit for memory specificity and generalization. *Science*
591 339, 1290-1295 (2013).
- 592 71. Yilmaz M, Meister M. Rapid innate defensive responses of mice to looming visual
593 stimuli. *Current Biology* 23, 2011-2015 (2013).
- 594 72. Yizhar O, et al. Neocortical excitation/inhibition balance in information processing
595 and social dysfunction. *Nature* 477, 171-178 (2011).
- 596 73. Zhang X, van den Pol AN. Rapid binge-like eating and body weight gain driven by
597 zona incerta GABA neuron activation. *Science* 356, 853-859 (2017).
- 598 74. Zhang Z, et al. Superior Colliculus GABAergic Neurons Are Essential for Acute Dark
599 Induction of Wakefulness in Mice. *Current Biology* 29, 637-644 e633 (2019).
- 600 75. Zhao ZD, et al. Zona incerta GABAergic neurons integrate prey-related sensory
601 signals and induce an appetitive drive to promote hunting. *Nature Neurosci.* 22,
602 921-932 (2019).

- 603 76. Zhou Z, et al. A VTA GABAergic Neural Circuit Mediates Visually Evoked Innate
604 Defensive Responses. *Neuron* 103, 473-488 e476 (2019).

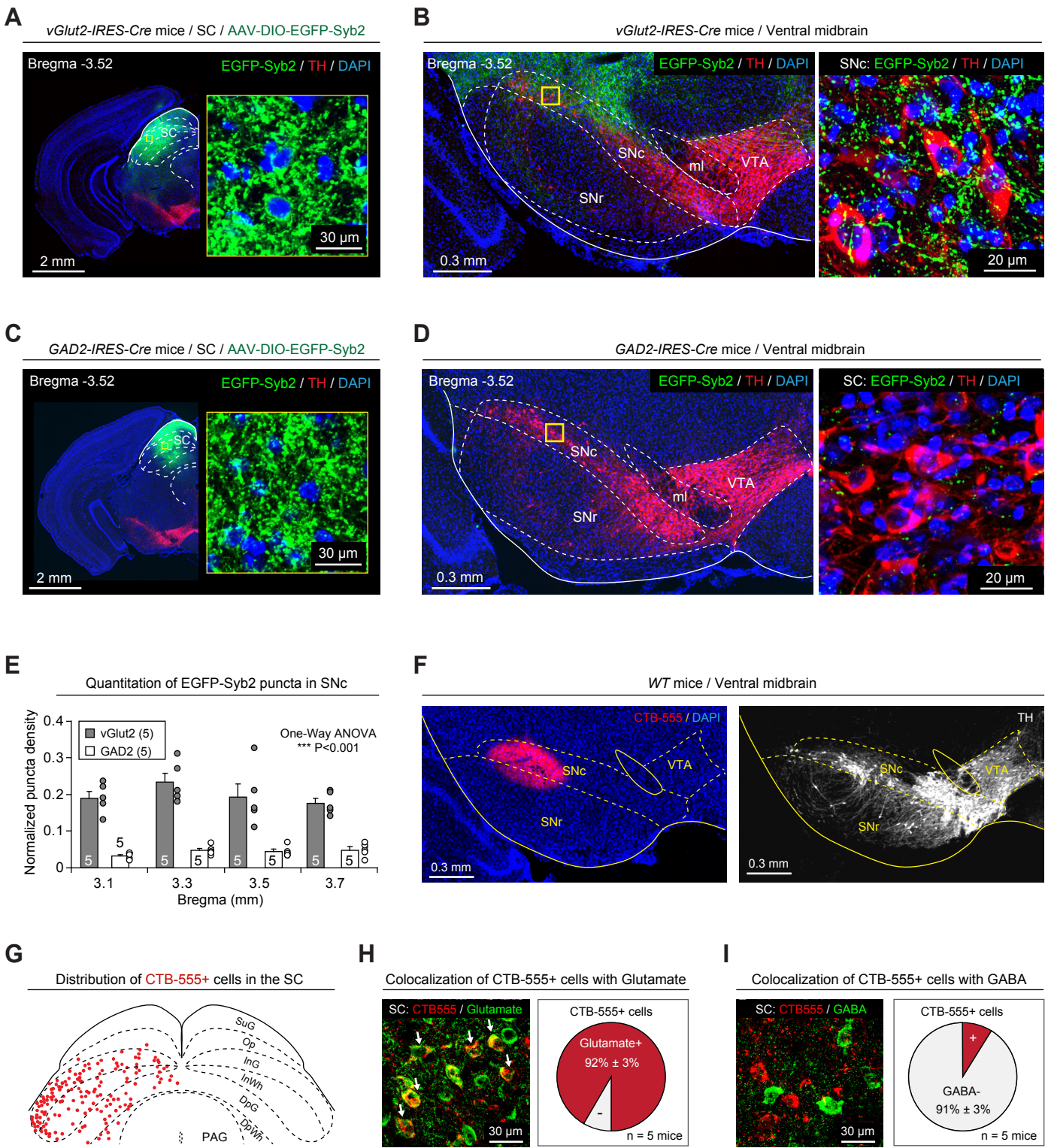


Figure 1 Huang et al., 2020

605 **LEGENDS**

606 **Figure 1 Cell-type-specific mapping of SC-SNc pathway.**

607 **(A, C)** Example coronal brain sections of *vGlut2-IRES-Cre* (A) and *GAD2-IRES-Cre* mice
608 (C) with EGFP-Syb2 expression in the SC. Insets, high-magnification micrographs
609 showing EGFP-Syb2+ puncta in the SC. **(B, D)** *Left*, EGFP-Syb2+ axon terminals in the
610 ventral midbrain of *vGlut2-IRES-Cre* (B) or *GAD2-IRES-Cre* mice (D). *Right*,
611 high-magnification micrographs showing EGFP-Syb2+ puncta (green) in the SNc. The
612 boundary of the SNc was delineated according to the immunofluorescence of TH (red).
613 **(E)** Normalized density of EGFP-Syb2+ puncta in the SNc of *vGlut2-IRES-Cre* (*vGlut2*)
614 and *GAD2-IRES-Cre* (*GAD2*) mice as a function of bregma. The normalization was
615 made by dividing the puncta density in the SNc with that in the SC. **(F)** An example
616 coronal section of ventral midbrain showing the injection of CTB-555 into the SNc of *WT*
617 mice (*left*). The boundaries of SNc and VTA were determined by immunofluorescence of
618 TH of dopamine neurons (*right*). **(G)** A schematic diagram showing the distribution of
619 SNc-projecting SC neurons that were labeled by CTB-555. For the raw image
620 corresponding to the schematic diagram, see Figure S1C. **(H, I)** Example micrographs
621 (*left*) and quantitative analyses (*right*) showing CTB-555+ cells in the SC are
622 predominantly positive for glutamate (H) and negative for GABA (I). Number of mice was
623 indicated in the graphs (E, H, I). Data in (E, H, I) are means \pm SEM (error bars).
624 Statistical analyses in (E) were performed by One-Way ANOVA (***) $P < 0.001$). For the *P*
625 values, see Table S4. Scale bars are indicated in the graphs.

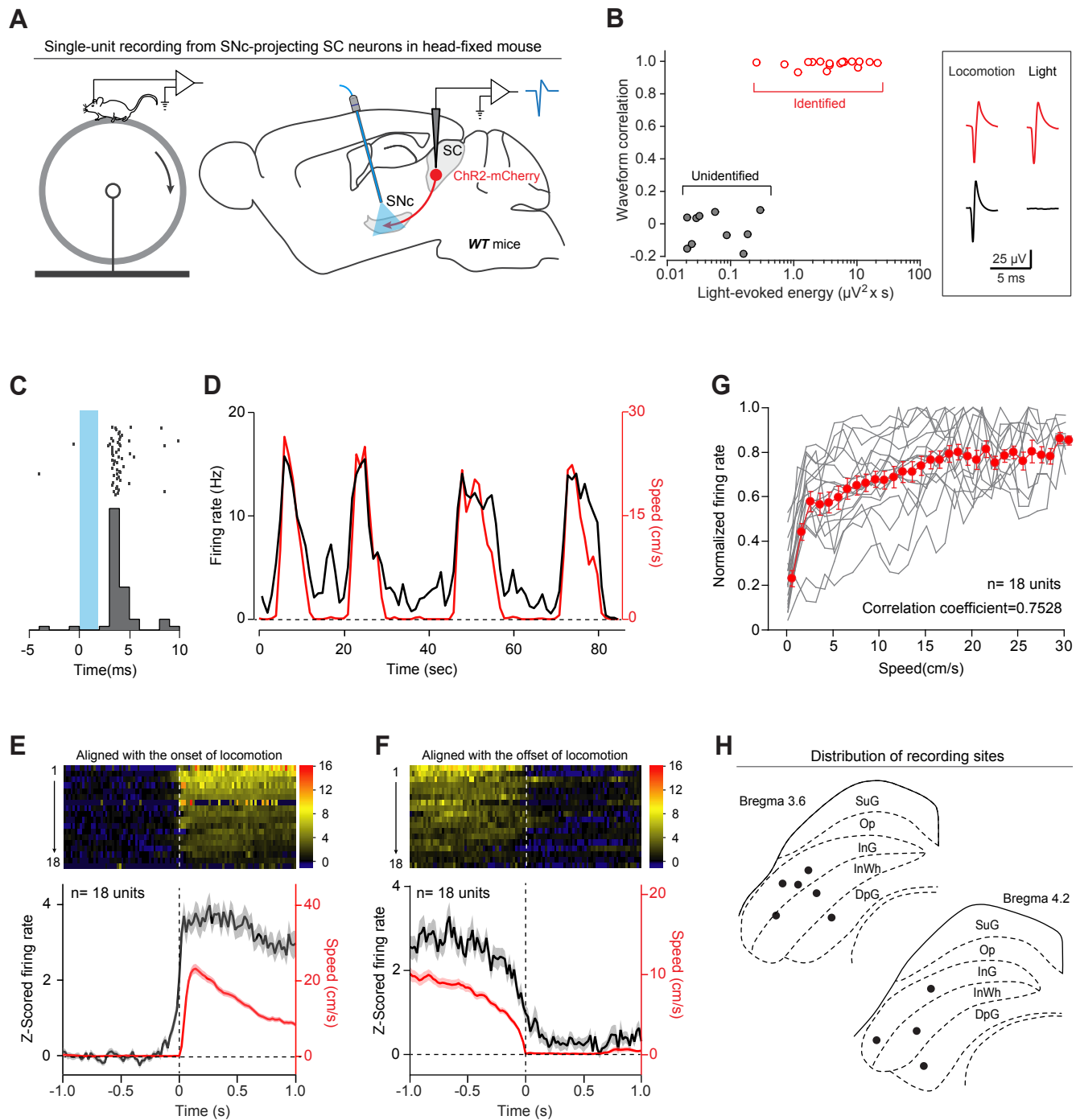


Figure 2 Huang et al., 2020

626 **Figure 2 SNc-projecting SC neurons encode locomotion speed.**

627 **(A)** Schematic diagram showing a head-fixed awake mouse walking on a cylindrical
628 treadmill (*left*) and antidromic activation strategy for single-unit recording from
629 SNc-projecting SC neurons (*right*). **(B)** Correlation analysis of action potentials of
630 individual units evoked either by light pulses (Light) or by locomotion (Locomotion),
631 confirming a segregation between antidromically identified units (red dots and traces)
632 and unidentified units (grey dots and traces). **(C)** Raster (*top*) and peristimulus time
633 histogram (PSTH, *bottom*) of an example putative SNc-projecting SC neurons showing a
634 latency of ~3 ms relative to the onset of light pulses. **(D)** Smoothed PSTH (trace in black)
635 of an example putative SNc-projecting SC neuron aligned with locomotion speed (trace
636 in red). **(E, F)** Heat-map graphs (*top*) and averaged time course (*bottom*) of Z-scored
637 firing rate of 18 putative SNc-projecting SC neurons aligned to the onset (E) and the
638 offset (F) of locomotion. **(G)** Averaged (red) and individual (gray) normalized
639 instantaneous firing rate during locomotion as a function of locomotion speed in 500 ms
640 bins. **(H)** Distribution of recording site (black dots) in the SC. For example micrograph,
641 see Figure S4C. Number of units was indicated in the graphs (E-G). Data in (E-G) are
642 means \pm SEM (error bars).

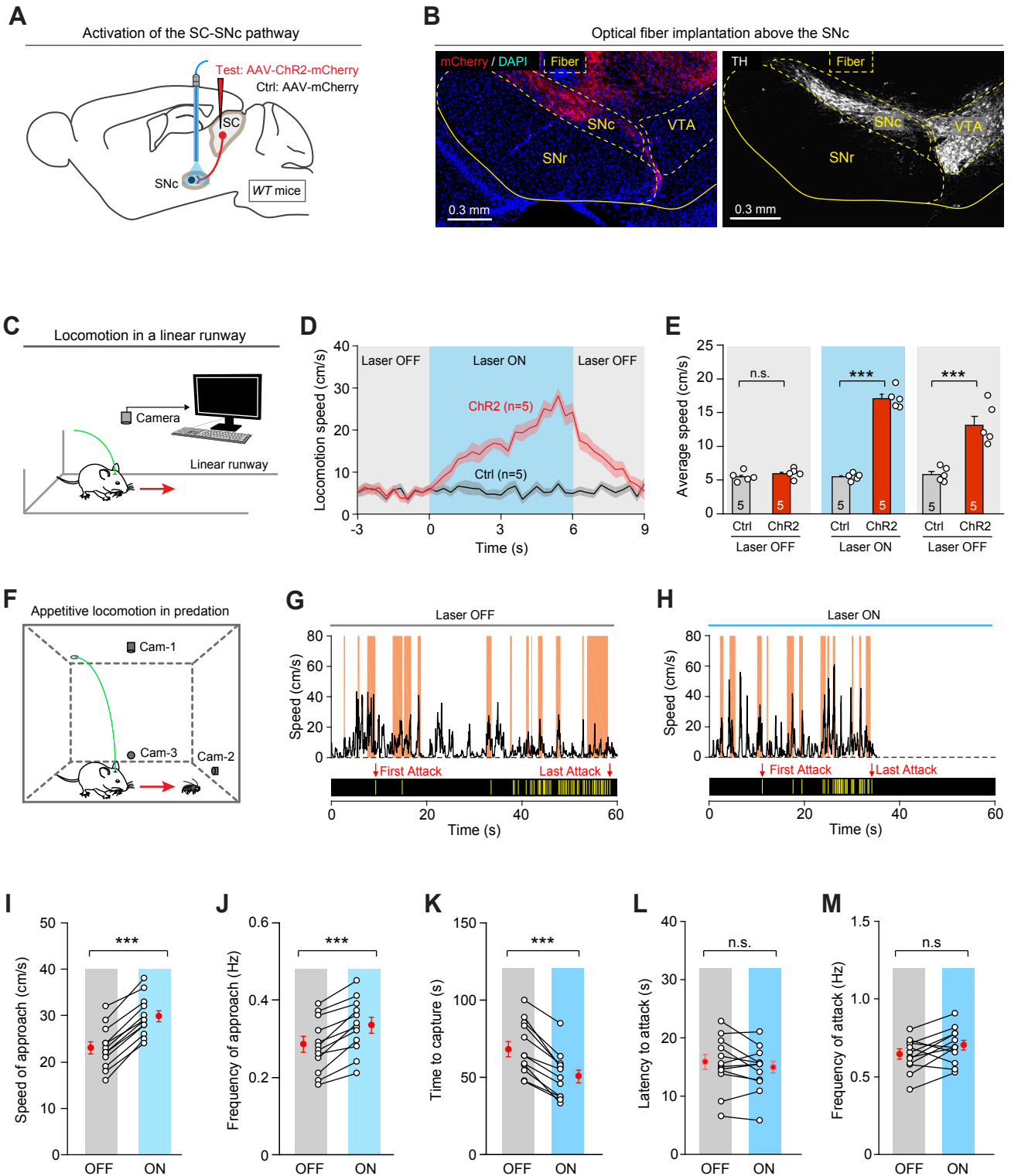


Figure 3 Huang et al., 2020

643 **Figure 3 Activation of the SC-SNc pathway promoted appetitive locomotion. (A)**
644 Schematic diagram showing injection of AAV-ChR2-mCherry into the SC of *WT* mice,
645 followed by optical fiber implantation above the SNc. For the example micrograph of
646 ChR2-mCherry expression in the SC, see Figure S5A. **(B)** An example coronal section of
647 ventral midbrain with an optical-fiber track above the ChR2-mCherry+ axon terminals in
648 the SNc (*left*), the boundary of which was delineated by the immunofluorescence of TH
649 (*right*). **(C)** Schematic diagram showing the experimental configuration to monitor mouse
650 locomotor behavior in the linear runway. **(D)** Time courses of locomotion speed of control
651 (Ctrl) and test mice (ChR2) in the linear runway before, during and after light stimulation
652 of the SC-SNc pathway (10 Hz, 10 ms, 6 s, 10 mW). **(E)** Quantitative analyses of
653 average locomotion speed of control (Ctrl) and test mice (ChR2) before, during and after
654 photostimulation of the SC-SNc pathway. For the dependence of locomotion speed on
655 the frequency of photostimulation, see Figure S5C. **(F)** Schematic diagram showing the
656 experimental configuration to monitor predatory hunting in the arena. **(G, H)** Time course
657 of locomotion speed (*top*) and jaw attacks (*bottom*) during predatory hunting of an
658 example mouse without (G) and with (H) photostimulation of the SC-SNc pathway (10 Hz,
659 10 ms, 10 mW). The shaded areas (orange) indicated the approach episodes in
660 predatory hunting. For the analyses of azimuth angle and PPD, see Figure S5F and S5G.
661 **(I-M)** Speed of approach (I), frequency of approach (J), time to capture (K), latency to
662 attack (L), and frequency of attack (M) in predatory hunting of mice without (OFF) and
663 with (ON) photostimulation of the SC-SNc pathway. Number of mice was indicated in the
664 graphs (D, E, I-M). Data in (D, E, I-M) are means \pm SEM (error bars). Statistical analyses
665 in (E, I-M) were performed by Student t-tests (n.s. $P > 0.1$; *** $P < 0.001$). For the P values,
666 see Table S4. Scale bars are indicated in the graphs.

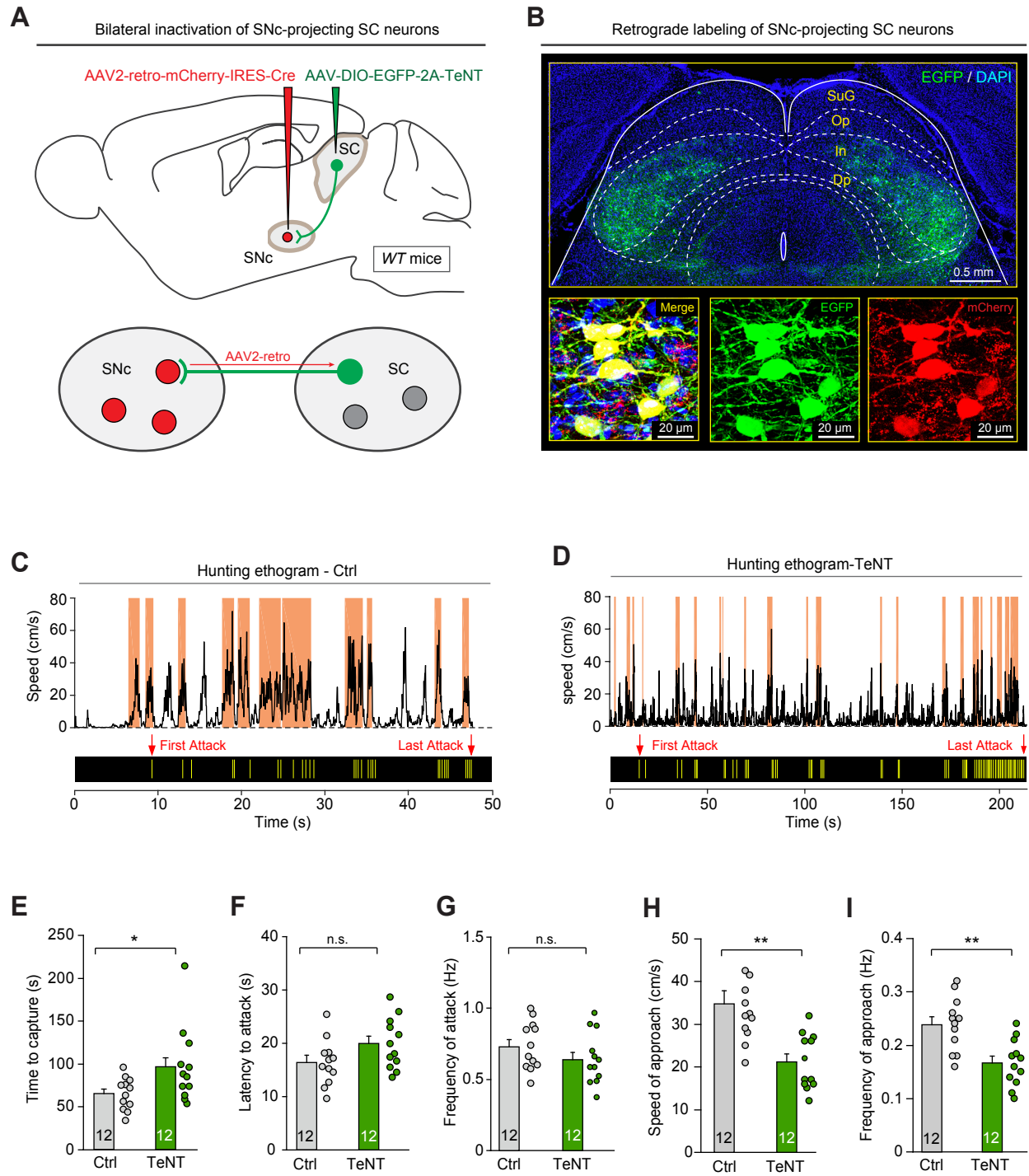


Figure 4 Huang et al., 2020

667 **Figure 4 The SC-SNc pathway is required for appetitive locomotion during**
668 **predatory hunting.**

669 **(A)** Schematic diagram showing the AAV2-retro strategy to selectively inactivate the
670 SNc-projecting SC neurons with TeNT. For the example coronal section of ventral
671 midbrain showing the injection of AAV2-retro-mCherry-IRES-Cre, see Figure S6A. **(B)** An
672 example coronal brain section showing EGFP⁺ SNc-projecting SC neurons distributed in
673 the intermediate layer (In) and deep layer (Dp) of SC. Inset, merged and single-channel
674 micrographs showing SNc-projecting SC neurons were dually labeled by mCherry and
675 EGFP. **(C, D)** Time course of locomotion speed (*top*) and jaw attacks (*bottom*) during
676 predatory hunting of example mice either without (C, Ctrl) or with (D, TeNT) synaptic
677 inactivation of SNc-projecting SC neurons. The shaded areas (orange) indicated the
678 approach episodes in predatory hunting. For the analyses of azimuth angle and PPD,
679 see Figure S6B and S6C. **(E-I)** Quantitative analyses of time to capture (E), latency to
680 attack (F), frequency of attack (G), speed of approach (H), and frequency of approach (I)
681 during predatory hunting in mice without (Ctrl) and with (TeNT) synaptic inactivation of
682 SNc-projecting SC neurons. Number of mice was indicated in the graphs (E-I). Data in
683 (E-I) are means \pm SEM (error bars). Statistical analyses in (E-I) were performed by
684 Student t-tests (n.s. $P > 0.1$; * $P < 0.05$; ** $P < 0.01$). For the P values, see Table S4. Scale
685 bars are indicated in the graphs.

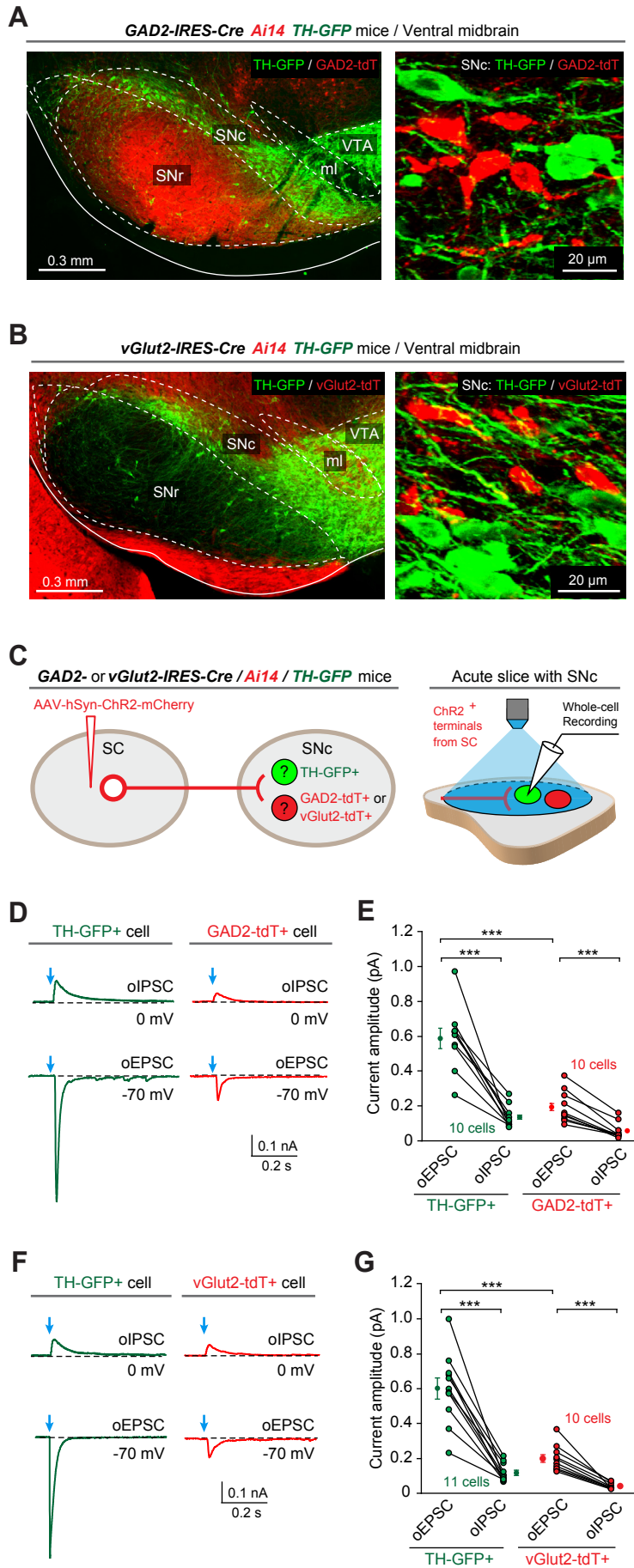


Figure 5 Huang et al., 2020

686 **Figure 5 Dopamine neurons are the primary postsynaptic target of the SC-SNc**
687 **pathway.**

688 **(A)** An example coronal section with ventral midbrain (*left*) and the high-magnification
689 micrograph (*right*) showing the segregation of GAD2-tdT+ neurons and TH-GFP+
690 neurons in the SNc of *GAD2-IRES-Cre/Ai14/TH-GFP* triple transgenic mice. **(B)** An
691 example coronal section with ventral midbrain (*left*) and the high-magnification
692 micrograph (*right*) showing the segregation of vGlut2-tdT+ neurons and TH-GFP+
693 neurons in the SNc of *vGlut2-IRES-Cre/Ai14/TH-GFP* triple transgenic mice. **(C)**
694 Schematic diagram showing injection of AAV-hSyn-ChR2-mCherry into the SC of
695 *GAD2-IRES-Cre/Ai14/TH-GFP* or *vGlut2-IRES-Cre/Ai14/TH-GFP* mice (*left*) and
696 whole-cell recording from TH-GFP+ (green), GAD2-tdT+ (red) or vGlut2-tdT+ (red)
697 neurons while illuminating ChR2-positive axon terminals from the SC (*right*). **(D, E)**
698 Example traces (D) and quantitative analyses (E) of oEPSCs and oIPSCs from
699 TH-GFP+ and GAD2-tdT+ neurons in the slices of *GAD2-IRES-Cre/Ai14/TH-GFP* mice.
700 **(F, G)** Example traces (F) and quantitative analyses (E) of oEPSCs and oIPSCs from
701 TH-GFP+ and vGlut2-tdT+ neurons in the slices of *vGlut2-IRES-Cre/Ai14/TH-GFP* mice.
702 Number of neurons is indicated in the graphs (E, G). Data in (E, G) are means \pm SEM
703 (error bars). Statistical analyses in (E, G) were performed by Student t-test (***) $P <$
704 0.001). For the P values, see Table S4. Scale bars are indicated in the graphs.

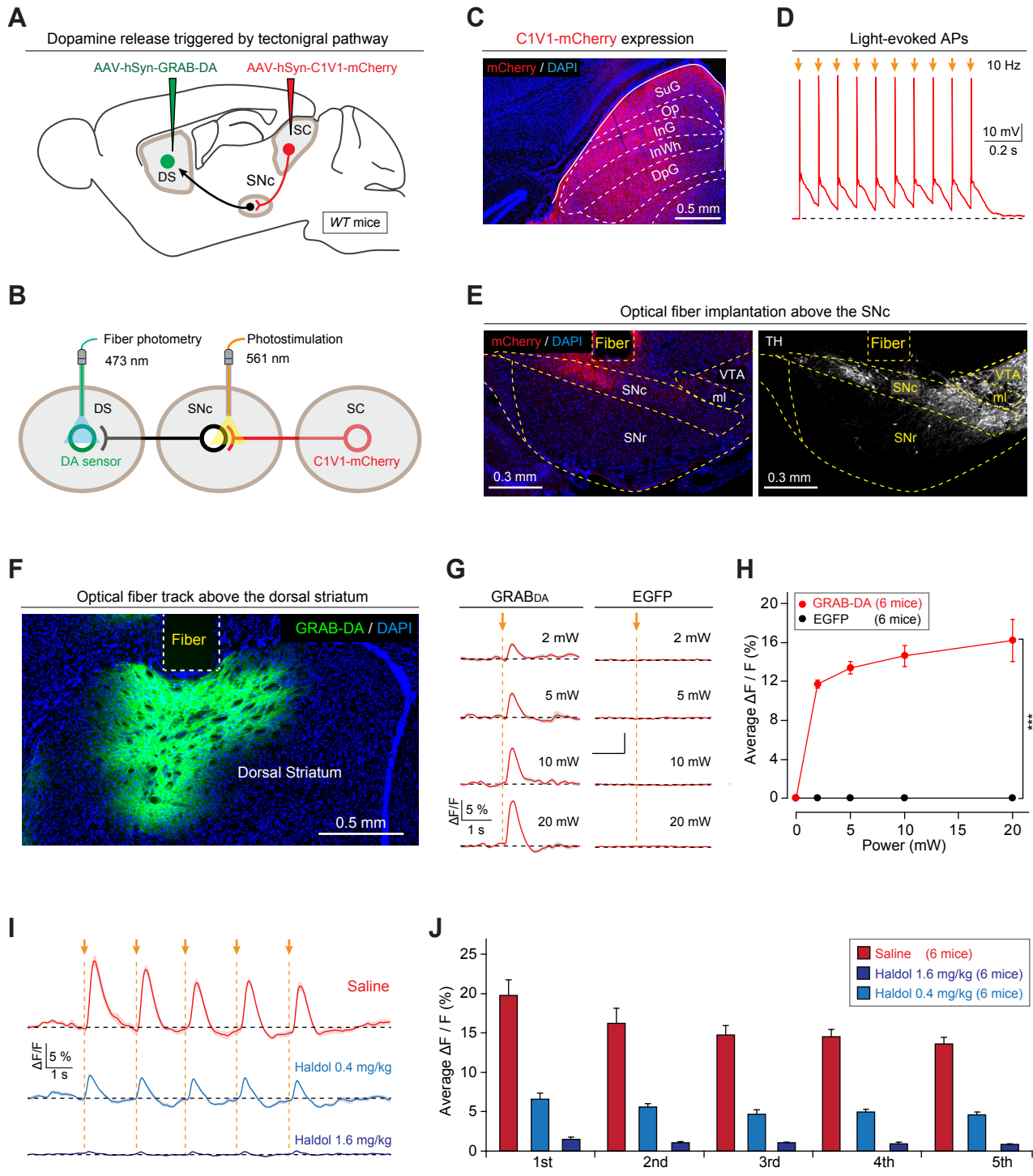


Figure 6 Huang et al., 2020

705 **Figure 6 Activation of the SC-SNc pathway triggers dopamine release in the dorsal**
706 **striatum.**

707 **(A)** Schematic diagram showing injections of AAV-hSyn-C1V1-mCherry in the SC and
708 AAV-hSyn-GRAB-DA in the dorsal striatum (DS) of *WT* mice. **(B)** Schematic diagram
709 showing implantation of optical fibers above the SNc and DS to apply photostimulation
710 and fiber photometry recording, respectively. **(C)** An example coronal section with
711 C1V1-mCherry expression in the SC. **(D)** In acute SC slices, light pulses (2 ms, 561 nm,
712 10 Hz, 10 pulses) illuminating on C1V1-mCherry+ SC neurons reliably triggered action
713 potential firing. **(E)** An example coronal section of ventral midbrain showing an
714 optical-fiber track above the C1V1-mCherry+ axon terminals in the SNc (*left*), the
715 boundary of which was determined according to the immunofluorescence of TH (*right*).
716 **(F)** An example coronal section with an optical-fiber track above the DS neurons
717 expressing GRAB-DA sensor. **(G, H)** Example traces (G) and input-output curve (H) of
718 GRAB-DA signals evoked by photostimulation of the SC-SNc pathway with different
719 laser power. EGFP was used as a control of GRAB-DA sensor. **(I, J)** Example traces (I)
720 and quantitative analyses (J) of GRAB-DA signals evoked by photostimulation (561 nm,
721 5 pulses, 2 ms, 0.5 Hz, 10 mW) of the SC-SNc pathway in mice treated with saline or
722 Haloperidol (0.4 or 1.6 mg/kg). Number of mice was indicated in the graphs (H, J). Data
723 in (H, J) are means \pm SEM (error bars). Statistical analyses in (H, J) were performed by
724 One-Way ANOVA (***) $P < 0.001$). For the P values, see Table S4. Scale bars are
725 indicated in the graphs.

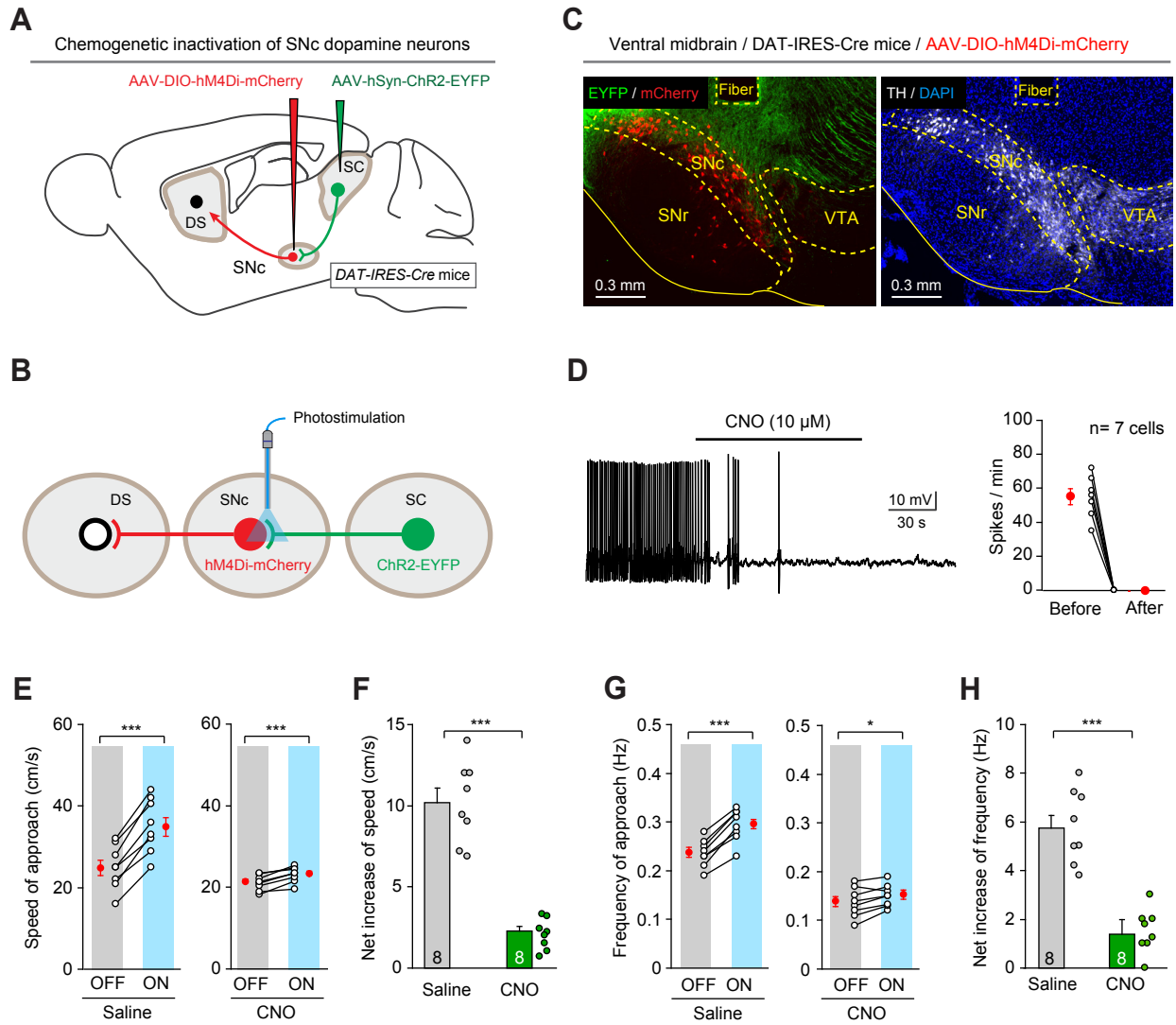


Figure 7 Huang et al., 2020

726 **Figure 7 SNc dopamine neurons mediated the effect of SC-SNc pathway**
727 **activation.**

728 **(A)** Schematic diagram showing injection of AAV-DIO-hM4Di-mCherry and
729 AAV-ChR2-EYFP into the SNc and SC of *DAT-IRES-Cre* mice. For an example coronal
730 section showing the expression of ChR2-EYFP in the SC, see Figure S8A. **(B)**
731 Schematic diagram showing implantation of an optical fiber above the SNc to apply light
732 stimulation on ChR2-EYFP+ axon terminals from the SC. **(C)** An example coronal
733 section of ventral midbrain showing the optical fiber track above the hM4Di-mCherry+
734 SNc dopamine neurons intermingled with ChR2-EYFP+ axons from the SC (*left*). The
735 boundaries of SNc and VTA were delineated by the immunofluorescence of TH (*right*). **(D)**
736 An example train of action potentials recorded from SNc dopamine neurons expressing
737 hM4Di-mCherry (*left*) and quantitative analyses of spike number per minute before and 3
738 min after perfusion of 10 μ M CNO in ACSF (*right*). **(E)** The effect of light stimulation of
739 the SC-SNc pathway on speed of approach during predatory hunting in mice treated with
740 saline (*left*) or CNO (*right*). **(F)** Chemogenetic suppression of SNc dopamine neurons
741 with CNO significantly attenuated the net effects of light stimulation of the SC-SNc
742 pathway on speed of approach during predatory hunting. **(G)** The effect of light
743 stimulation of the SC-SNc pathway on frequency of approach during predatory hunting in
744 mice treated with saline (*left*) or CNO (*right*). **(H)** Chemogenetic suppression of SNc
745 dopamine neurons with CNO significantly attenuated the net effects of light stimulation of
746 the SC-SNc pathway on frequency of approach during predatory hunting. Number of
747 cells (D) and mice (E-H) was indicated in the graphs. Data in (D-H) are means \pm SEM
748 (error bars). Statistical analyses in (D-H) were performed by Student t-tests (n.s. $P > 0.1$; *
749 $P < 0.05$; *** $P < 0.001$). For the P values, see Table S4. Scale bars are indicated in the
750 graphs.

751 **MATERIALS AND METHODS**

752 **Animals**

753 All experimental procedures were conducted following protocols approved by the
754 Administrative Panel on Laboratory Animal Care at the National Institute of Biological
755 Sciences, Beijing (NIBS). The *vGlut2-IRES-Cre* (Vong et al., 2011), *GAD2-IRES-Cre*
756 (Taniguchi et al., 2011), *DAT-IRES-Cre* (Backman et al., 2006), and *Ai14* (Madisen et al.,
757 2010) mouse lines were imported from the Jackson Laboratory (JAX Mice and Services).
758 Mice were maintained on a circadian 12-h light/12-h dark cycle with food and water
759 available ad libitum. Mice were housed in groups (3–5 animals per cage) before they
760 were separated 3 days prior to virus injection. After virus injection, each mouse was
761 housed in one cage for 3 weeks before subsequent experiments. To avoid potential
762 sex-specific differences, we used male mice only.

763

764 **AAV vectors**

765 Two AAV serotypes (AAV-DJ, AAV2-retro) were used. The AAVs used in the present
766 study are listed in Table S1. The viral particles were purchased from Shanghai Taitool
767 Bioscience Inc. and Brain VTA Inc. The viral vector titers before dilution were in the range
768 of $0.8\text{--}1.5 \times 10^{13}$ viral particles/ml. The final titer used for AAV injection is 5×10^{12} viral
769 particles/ml.

770

771 **Stereotaxic injection**

772 Mice were anesthetized with an intraperitoneal injection of tribromoethanol
773 (125–250 mg/kg). Standard surgery was performed to expose the brain surface above
774 the superior colliculus (SC), substantia nigra pars compacta (SNc), ventral tegmental
775 area (VTA), zona incerta (ZI) or dorsal striatum (DS). Coordinates used for SC injection
776 were as follows: bregma -3.60 mm, lateral \pm 1.30 mm, and dura -1.75 mm. Coordinates

777 used for SNc injection were as follows: bregma -3.40 mm, lateral \pm 1.25 mm, and dura
778 -4.00 mm. Coordinates used for VTA injection were as follows: bregma -3.40 mm, lateral
779 \pm 0.50 mm, and dura -4.00 mm. Coordinates used for DS injection were as follows:
780 bregma 0.74 mm, lateral \pm 1.50 mm, and dura -2.40 mm. Coordinates used for ZI
781 injection were: bregma -2.00 mm, lateral \pm 1.25 mm and dura -4.25 mm. The AAVs and
782 CTB were stereotaxically injected with a glass pipette connected to a Nano-liter Injector
783 201 (World Precision Instruments, Inc.) at a slow flow rate of 0.15 μ l / min to avoid
784 potential damage to local brain tissue. The pipette was withdrawn at least 20 min after
785 viral injection.

786 For optogenetic activation and synaptic inactivation experiments, AAV injections
787 were bilateral. For anterograde and retrograde tracing experiments, CTB injection was
788 unilateral. Histological analyses were conducted one week (for CTB) and at least three
789 weeks (for AAV) after injection. Experimental designs related to viral injection are
790 summarized in Table S2.

791

792 **Optical fiber implantation**

793 Thirty minutes after AAV injection, a ceramic ferrule with an optical fiber (230 μ m in
794 diameter, numerical aperture = 0.37) was implanted with the fiber tip on top of the SNc
795 (bregma -3.40 mm, lateral \pm 1.25 mm, dura -3.80 mm) or the dorsal striatum (bregma
796 0.74 mm, lateral \pm 1.50 mm, and dura -2.20 mm). The ferrule was then secured on the
797 skull with dental cement. After implantation, the skin was sutured, and antibiotics were
798 applied to the surgical wound. The optogenetic experiments were conducted 3 weeks
799 after optical fiber implantation. All experimental designs related to optical fiber
800 implantation are summarized in Table S2. For optogenetic stimulation, the output of the
801 laser was measured and adjusted to 2, 5, 10, 15 and 20 mW before each experiment.
802 The pulse onset, duration, and frequency of light stimulation were controlled by a
803 programmable pulse generator attached to the laser system.

804

805 **Single-unit recording**

806 Antidromic activation strategy was used to identify the single-unit activity of
807 SNc-projecting SC neurons. AAV-hSyn-ChR2-mCherry was injected into the SC of
808 wild-type mice, followed by an optical fiber implanted above the SNc. Three weeks after
809 viral injection, single-unit recording was performed with a tungsten electrode in the SC of
810 head-fixed awake mouse. The tungsten electrode was vertically advanced into the lateral
811 SC with a Narishige micro-manipulator. The spikes were amplified by a differential
812 amplifier (Model 1800, A-M Systems, Everett, WA, USA), digitized (10 kHz) and stored
813 by Spike2 software (Version 7.03). When the single-unit activity was isolated, we tested
814 if the units were from SNc-projecting SC neurons. The putative SNc-projecting SC
815 neurons were identified by the antidromic spikes evoked by light-pulses (473 nm, 1 ms, 2
816 mW) illuminating ChR2-mCherry+ axon terminals in the SNc. The antidromically evoked
817 spikes had to conform to two criteria: first, their latency to the light pulse should be less
818 than 5 ms; second, their waveform should be similar to that of spikes evoked by
819 locomotion (Figure 2B). Only units with spikes faithfully following the light stimulations
820 with latency less than 5 ms were further tested for locomotion-correlated activity (Figure
821 2C). The spike sorting was performed with Spike2 Software (Version 7.03). For a certain
822 train of action potential, after setting the threshold of the spikes, Spike2 automatically
823 generated the templates and performed the spike-sorting. The quality of spike clustering
824 was further confirmed by principal component analysis (Figure S4B). The single-unit
825 activity of SNc-projecting SC units was recorded with simultaneously measuring the
826 instantaneous locomotion speed of mice walking on the treadmill (Nanjing Thinktech
827 Inc.).

828

829 **Verification of recording sites**

830 The recording sites of the putative SNc-projecting SC neurons were marked with

831 electrolytic lesions applied by passing positive currents (40 μ A, 10 s) through the
832 tungsten electrode. Under deep anesthesia with urethane, the brain was perfused with
833 saline and PBS containing 4% PFA. After regular histological procedure, frozen sections
834 were cut at 40 μ m in thickness and counterstained with DAPI for histological verification
835 of recording sites.

836

837 **Preparation of behavioral tests**

838 After AAV injection and fiber implantation, the mice were housed individually for 3
839 weeks before the behavioral tests. Before the behavioral tests, they were handled daily
840 by the experimenters for at least 3 days. On the day of the behavioral test, the mice were
841 transferred to the testing room and were habituated to the room conditions for 3 h before
842 the experiments started. The apparatus was cleaned with 20% ethanol to eliminate odor
843 cues from other mice. All behavioral tests were conducted during the same circadian
844 period (13:00–19:00). All behaviors were scored by the experimenters, who were blind to
845 the animal treatments.

846

847 **Behavioral paradigm for predatory hunting**

848 The procedure of predatory hunting experiment was described previously (Shang et
849 al., 2019). Before the predatory hunting test, the mice went through a 9-day habituation
850 procedure (Day H1–H9). On each of the first three habituation days (Day H1, H2, H3),
851 three cockroaches were placed in the home-cage (with standard chow) of mice at 2:00
852 PM. The mice readily consumed the cockroaches within 3 h after cockroach appearance.
853 On Day H3, H5, H7, and H9, we initiated 24-h food deprivation at 7:00 PM by removing
854 chow from the home-cage. On Day H4, H6, and H8 at 5:00 PM, we let the mice freely
855 explore the arena (25 cm x 25 cm) for 10 min, followed by three trials of hunting practice
856 for the cockroach. After hunting practice, we put the mice back in their home-cages and
857 returned the chow at 7:00 PM. On the test day, we let the mice freely explore the arena

858 for 10 min, followed by three trials of predatory hunting. After the tests, the mice were put
859 back in their home-cage, followed by the return of chow. The cockroach was purchased
860 from a merchant in Tao-Bao Online Stores (www.taobao.com).

861 Before the hunting practice or test, the mice were transferred to the testing room and
862 habituated to the room conditions for 3 h before the experiments started. The arena was
863 cleaned with 20% ethanol to eliminate odor cues from other mice. All behaviors were
864 scored by the experimenters, who were blind to the animal treatments. Hunting
865 behaviors were measured in an arena (20 cm × 20 cm, square open field) without regular
866 mouse bedding. After entering, the mice explored the arena for 10 min, followed by the
867 introduction of a cockroach. For each mouse, predatory hunting was repeated for three
868 trials. Each trial began with the introduction of prey to the arena. The trial ended when
869 the predator finished ingesting the captured prey. After the mice finished ingesting the
870 prey body, debris was removed before the new trial began.

871

872 **Measurement of appetitive locomotion and predatory attack in predatory hunting**

873 In the paradigm of predatory hunting, mouse behavior was recorded in the arena with
874 three orthogonally positioned cameras (50 frames/sec; Point Grey Research, Canada).
875 With the video taken by the overhead camera, the instantaneous head orientation of
876 predator relative to prey (azimuth angle) and predator-prey distance (PPD) was analyzed
877 with the Software EthoVision XT 14 (Noldus Information Technology). The episode of
878 approach was identified by two empirical criteria (Hoy et al., 2016). First, the PPD should
879 continuously decrease until it is less than 3 cm. Second, the azimuth angle of mouse
880 head to cockroach should be within the range of -90 deg to +90 deg. In WT mice, each
881 trial of predatory hunting contains 10~20 episodes of approach. Speed of approach and
882 frequency of approach were used to quantitatively measure the appetitive locomotion in
883 the episodes of approach. Speed of approach of each mouse was calculated by
884 averaging the peak speed in all the approach episodes in the trial. Frequency of

885 approach was the total number of approach episodes divided by the time to prey capture
886 in the trial.

887 With the videos taken by the two horizontal cameras, we carefully identified
888 predatory attacks with jaw by replaying the video frame by frame (50 frames/sec). We
889 marked the predatory jaw attacks with yellow vertical lines in the behavioral ethogram of
890 predatory hunting. With this method, we measured three parameters of predatory
891 hunting: time to prey capture, latency to jaw attack, and frequency of jaw attack. Time to
892 prey capture was defined as the time between the introduction of prey and the last jaw
893 attack. Latency to jaw attack was defined as the time between the introduction of the
894 prey and the first jaw attack from the predator. Frequency of jaw attack was defined as
895 the number of jaw attacks divided by time to prey capture. Data for three trials were
896 averaged.

897

898 **Measurement of defensive locomotion triggered by looming visual stimuli**

899 Measurement of defensive locomotion triggered by looming visual stimulus was
900 described previously (Shang et al., 2018). Briefly, defensive locomotion was measured in
901 an arena (35 cm × 35 cm, square open field) with corn-cob bedding. No shelter was
902 provided. A regular computer monitor was positioned above the arena for presentation of
903 overhead looming visual stimuli. After entering, the mice explored the arena for 10 min.
904 This was followed by the presentation of three cycles of overhead looming visual stimuli
905 consisting of an expanding dark disk. The visual angle of the dark disk was expanded
906 from 2 to 20 degrees within 250 ms. Luminance of the dark disk and background were
907 0.1 and 3.6 cd/m², respectively. Mouse behavior was recorded (50 frames/sec; Point
908 Grey Research, Canada) by two orthogonally positioned cameras with LEDs providing
909 infrared illumination. The instantaneous location of the mouse in the arena was
910 measured by a custom-written Matlab program. The instantaneous locomotion speed
911 was calculated with a 200 ms time-bin. The Matlab code is available upon request.

912

913 **Measurement of locomotion in linear runway**

914 Mouse behavior was recorded in the linear runway (10 cm x 16 cm x 120 cm) with
915 an overhead camera (50 frames/sec; Point Grey Research, Canada). With the video
916 taken by the overhead camera, we measured the instantaneous locomotion speed with
917 the Software EthoVision XT 14 (Noldus Information Technology).

918

919 **Slice physiological recording**

920 Preparation of acute brain slices was performed according to the published work
921 (Liu et al., 2017). Brain slices containing the SC or SNc were prepared from adult mice
922 anesthetized with isoflurane before decapitation. Brains were rapidly removed and
923 placed in ice-cold oxygenated (95% O₂ and 5% CO₂) cutting solution (228 mM sucrose,
924 11 mM glucose, 26 mM NaHCO₃, 1 mM NaH₂PO₄, 2.5 mM KCl, 7 mM MgSO₄, and 0.5
925 mM CaCl₂). Coronal brain slices (400 µm) were cut using a vibratome (VT 1200S, Leica
926 Microsystems, Wetzlar, Germany). The slices were incubated at 28°C in oxygenated
927 artificial cerebrospinal fluid (ACSF: 125 mM NaCl, 2.5 mM KCl, 1.25 mM NaH₂PO₄, 1.0
928 mM MgCl₂, 25 mM NaHCO₃, 15 mM glucose, and 2.0 mM CaCl₂) for 30 min (~305
929 mOsm, pH 7.4). The slices were then kept at room temperature under the same
930 conditions for 30 min before transfer to the recording chamber at room temperature. The
931 ACSF was perfused at 1 ml/min. The acute brain slices were visualized with a 40×
932 Olympus water immersion lens, differential interference contrast (DIC) optics (Olympus
933 Inc., Japan), and a CCD camera.

934 Patch pipettes were pulled from borosilicate glass capillary tubes (Cat #64-0793,
935 Warner Instruments, Hamden, CT, USA) using a PC-10 pipette puller (Narishige Inc.,
936 Tokyo, Japan). For recording of postsynaptic currents (voltage clamp), pipettes were
937 filled with solution (126 mM Cs-methanesulfonate, 10 mM HEPES, 1 mM EGTA, 2 mM
938 QX-314 chloride, 0.1 mM CaCl₂, 4 mM Mg-ATP, 0.3 mM Na-GTP, 8 mM

939 Na-Phosphocreatine, pH 7.3 adjusted with CsOH, ~290 mOsm) (Kim et al., 2015). For
940 recording of action potentials (current clamp), pipettes were filled with solution (135 mM
941 K-methanesulfonate, 10 mM HEPES, 1 mM EGTA, 1 mM Na-GTP, 4 mM Mg-ATP, pH
942 7.4). The resistance of pipettes varied between 3.0–3.5 M Ω . The current and voltage
943 signals were recorded with MultiClamp 700B and Clampex 10 data acquisition software
944 (Molecular Devices). After establishment of the whole-cell configuration and equilibration
945 of the intracellular pipette solution with the cytoplasm, series resistance was
946 compensated to 10–15 M Ω . Recordings with series resistances of > 15 M Ω were
947 rejected. An optical fiber (230 μ m in diameter) was used to deliver light pulses, with the
948 fiber tip positioned 500 μ m above the brain slices. Laser power was adjusted to 2, 5, 10,
949 or 20 mW. Light-evoked action potentials from ChR2-mCherry+ neurons in the SC were
950 triggered by a light-pulse train (473 nm, 2 ms, 10 Hz, 20 mW) synchronized with
951 Clampex 10 data acquisition software (Molecular Devices). Light-evoked postsynaptic
952 currents from SNc neurons were triggered by single light pulses (2 ms) in the presence
953 of 4-aminopyridine (4-AP, 20 μ M) and tetrodotoxin (TTX, 1 μ M). D-AP5 (50 μ M)/CNQX
954 (20 μ M) or picrotoxin (PTX, 50 μ M) were perfused with ACSF to examine the
955 neurotransmitter/receptor type of optically-evoked postsynaptic currents.

956

957 **Fiber photometry**

958 A fiber photometry system (ThinkerTech, Nanjing, China) was used for recording
959 GRAB_{DA} signals from genetically identified neurons (Sun et al., 2018). To induce
960 fluorescence signals, a laser beam from a laser tube (488 nm) was reflected by a
961 dichroic mirror, focused by a 10 \times lens (N.A. 0.3) and coupled to an optical commutator. A
962 2-m optical fiber (230 μ m in diameter, N.A. 0.37) guided the light between the
963 commutator and implanted optical fiber. To minimize photo bleaching, the power
964 intensity at the fiber tip was adjusted to 0.02 mW. The GRAB_{DA} fluorescence was
965 band-pass filtered (MF525-39, Thorlabs) and collected by a photomultiplier tube (R3896,

966 Hamamatsu). An amplifier (C7319, Hamamatsu) was used to convert the photomultiplier
967 tube current output to voltage signals, which were further filtered through a low-pass filter
968 (40 Hz cut-off; Brownlee 440). The analogue voltage signals were digitalized at 100 Hz
969 and recorded by a Power 1401 digitizer and Spike2 software (CED, Cambridge, UK).

970 AAV-DJ-hSyn-GRAB-DA was stereotaxically injected into the dorsal striatum of *WT*
971 mice followed by optical fiber implantation above the injected site (see “Stereotaxic
972 injection” and “Optical fiber implantation”). Two weeks after AAV injection, fiber
973 photometry was used to record GRAB-DA signals from the cell bodies of dorsal striatum
974 neurons in freely moving mice. A flashing LED triggered by a 1-s square-wave pulse was
975 simultaneously recorded to synchronize the video and GRAB-DA signals. For recordings
976 from freely moving mice, mice with optical fibers connected to the fiber photometry
977 system freely explored the arena for 10 min. After the experiments, the optical fiber tip
978 sites above the dorsal striatum neurons were histologically examined in each mouse.

979

980 **Histological procedures**

981 Mice were anesthetized with isoflurane and sequentially perfused with saline and
982 phosphate buffered saline (PBS) containing 4% paraformaldehyde (PFA). Brains were
983 removed and incubated in PBS containing 30% sucrose until they sank to the bottom.
984 Post-fixation of the brain was avoided to optimize immunohistochemistry of GABA and
985 glutamate. Cryostat sections (40 μ m) containing the SC, SNc or DS were collected,
986 incubated overnight with blocking solution (PBS containing 10% goat serum and 0.7%
987 Triton X-100), and then treated with primary antibodies diluted with blocking solution for
988 3–4 h at room temperature. Primary antibodies used for immunohistochemistry are
989 displayed in Table S1. Primary antibodies were washed three times with washing buffer
990 (PBS containing 0.7% Triton X-100) before incubation with secondary antibodies (tagged
991 with Cy2, Cy3, or Cy5; dilution 1:500; Life Technologies Inc., USA) for 1 h at room
992 temperature. Sections were then washed three times with washing buffer, stained with

993 DAPI, and washed with PBS, transferred onto Super Frost slides, and mounted under
994 glass coverslips with mounting media.

995 Sections were imaged with an Olympus (Japan) VS120 epifluorescence microscope
996 (10× objective lens) or an Olympus FV1200 laser scanning confocal microscope (20×
997 and 60× oil-immersion objective lens). Samples were excited by 488, 543, or 633 nm
998 lasers in sequential acquisition mode to avoid signal leakage. Saturation was avoided by
999 monitoring pixel intensity with Hi-Lo mode. Confocal images were analyzed with ImageJ
1000 software.

1001

1002 **Quantification of synaptic puncta density**

1003 The micrographs used for measuring puncta density of SynaptoTag (Figure 1, B and
1004 D) were acquired with a 63× objective of Zeiss confocal system and analyzed with NIH
1005 Image J. The analysis of the synaptic puncta was described previously (Cao et al., 2013).
1006 In brief, the scale of micrographs was set in NIH Image J based on the physical
1007 dimension of micrographs acquired by Zeiss confocal system. After converting the
1008 micrographs from RGB color mode to 16-bit mode, the puncta in micrographs were
1009 binarized and the puncta density was measured automatically by NIH Image J. Then the
1010 puncta density in the SNc of each mouse was normalized by dividing with that in the
1011 intermediate layer of the lateral SC (Figure 1E).

1012

1013 **Cell-counting strategies**

1014 Cell-counting strategies are summarized in Table S3. For counting cells in the SC,
1015 we collected 40- μ m coronal sections from bregma -3.28 to bregma -4.48 for each mouse.
1016 Six sections evenly spaced by 200 μ m were sampled for immunohistochemistry to label
1017 cells positive for different markers. We acquired micrographs (10× objective, Olympus
1018 FV1200 microscope, Japan) within intermediate and deep layers of the SC followed by
1019 cell counting with ImageJ software. We calculated the percentages of glutamate+ and

1020 GABA+ neurons in the neuronal population retrogradely labeled by CTB-555. For
1021 counting cells in the SNc, we collected coronal sections (40 μ m) from bregma -2.80 to
1022 bregma -3.80 for each mouse. Five sections evenly spaced by 200 μ m were sampled for
1023 immunohistochemistry to label SNc cells positive for different markers. After image
1024 acquisition, we outlined the SC and SNc followed by cell counting with ImageJ software.
1025 The boundary of SNc in coronal sections was identified based on TH staining.

1026

1027 **DATA QUANTIFICATION AND STATISTICAL ANALYSIS**

1028 All experiments were performed with anonymized samples in which the
1029 experimenter was unaware of the experimental conditions of the mice. For the statistical
1030 analyses of experimental data, Student t-test and One-Way ANOVA were used. The “n”
1031 used for these analyses represents number of mice or cells. See the detailed information
1032 of statistical analyses in figure legend and in Table S4.

1033

1034 **DATA AND CODE AVAILABILITY**

1035 The data that support the findings of this study are available from the corresponding
1036 author upon reasonable request. The MATLAB code for data analyses is available from
1037 the corresponding author upon request.

1038

1039 77. Liu Z, et al. IGF1-Dependent Synaptic Plasticity of Mitral Cells in Olfactory Memory
1040 during Social Learning. *Neuron* 95, 106-122 e105 (2017).

1041 78. Shang C, et al. Divergent midbrain circuits orchestrate escape and freezing
1042 responses to looming stimuli in mice. *Nature Communications* 9, 1232 (2018).

1043 79. Cao P, et al., Complexin activates exocytosis of distinct secretory vesicles controlled
1044 by different synaptotagmins. *Journal of Neuroscience* 33 (4), 1714-1727 (2013)

Supplementary Materials

The SC-SNc pathway boosts appetitive locomotion in predatory hunting

Meizhu Huang, Dapeng Li, Qing Pei, Zhiyong Xie, Huating Gu, Aixue Liu, Zijun Chen, Yi Wang, Fangmiao Sun, Yulong Li, Jiayi Zhang, Miao He, Yuan Xie, Fan Zhang, Xiangbing Qi, Congping Shang, Peng Cao

This file includes:

Figure S1 to Figure S8

Movies S1 to S7

Tables S1 to S4

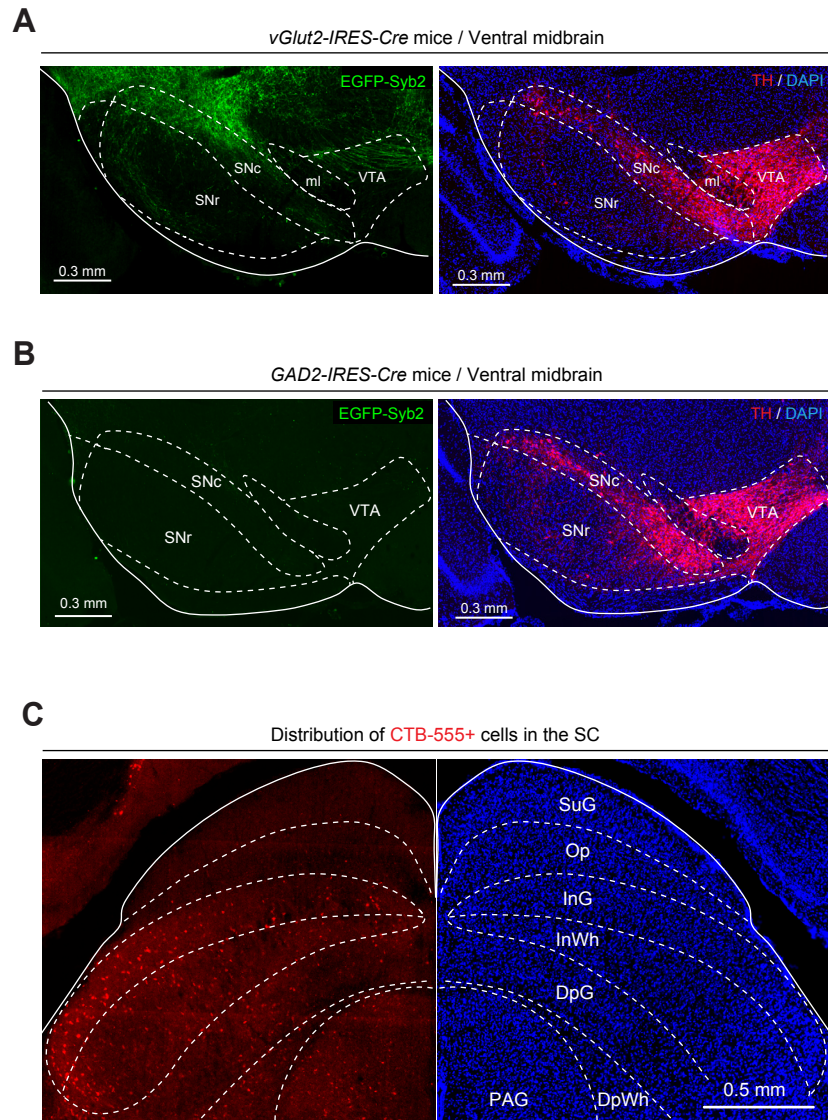


Figure S1 Huang et al., 2020

1 **Figure S1 Cell-type-specific mapping of tectonigral pathway.** (Related to Figure 1)

2 **(A, B)** Single-channel and merged micrographs showing EGFP-Syb2+ axon terminals in
3 the ventral midbrain of *vGlut2-IRES-Cre* (A) and *GAD2-IRES-Cre* mice (B). The
4 boundaries of SNc and VTA were determined by immunostaining of tyrosine hydroxylase
5 (TH, red) for dopamine neurons. **(C)** An example coronal section of the SC showing the
6 distribution of SNc-projecting SC neurons that were labeled by CTB-555. Scale bars
7 were indicated in the graphs.

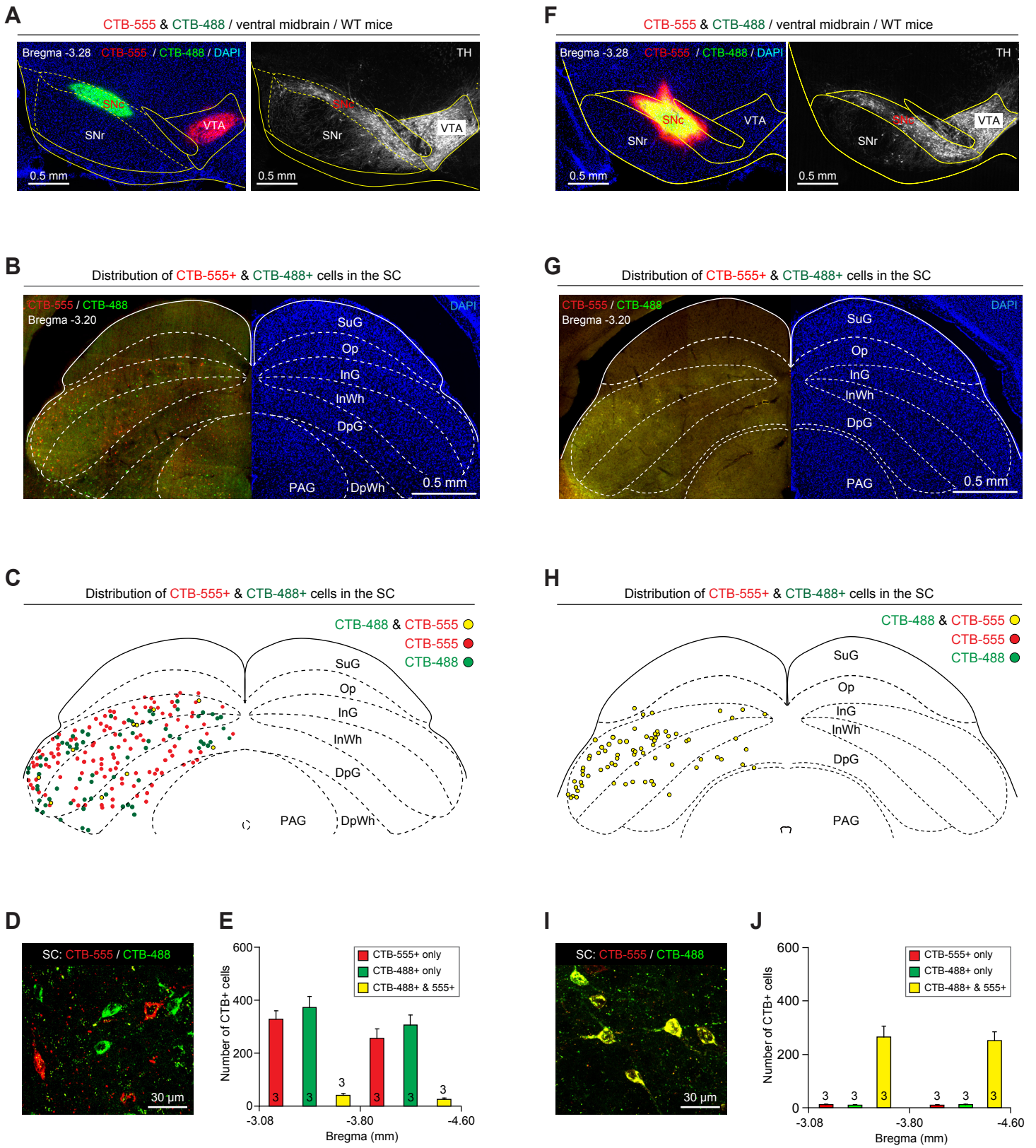


Figure S2 Huang et al., 2020

8 **Figure S2 SC-SNc pathway and SC-VTA pathway are anatomically segregated.**

9 (Related to Figure 1)

10 **(A)** Example coronal section of the ventral midbrain showing injection of CTB-488 and
11 CTB-555 into the SNc and VTA (*left*), the boundaries of which were delineated according
12 to the immunofluorescence of TH (*right*). **(B, C)** An example coronal section of the SC (B)
13 and the corresponding illustration (C) showing the distribution of CTB-555+ & CTB-488+
14 cells in the SC. **(D, E)** Example micrograph (D) and quantitative analyses (E) showing
15 CTB-555+ & CTB-488+ SC neurons were largely segregated. **(F)** Example coronal
16 section of the ventral midbrain showing injection of mixed CTB-488 & CTB-555 into the
17 SNc (*left*), the boundary of which was delineated according to the immunofluorescence
18 of TH (*right*). **(G, H)** An example coronal section of the SC (G) and the corresponding
19 illustration (H) showing the distribution of CTB-555+ & CTB-488+ cells in the SC. **(I, J)**
20 Example micrograph (I) and quantitative analyses (J) showing the retrogradely labeled
21 SC neurons are mostly positive for both CTB-555 and CTB-488. Numbers of mice (E and
22 J) are indicated in the graphs. Data in (E and J) are means \pm SEM. Scale bars are
23 labeled in the graphs.

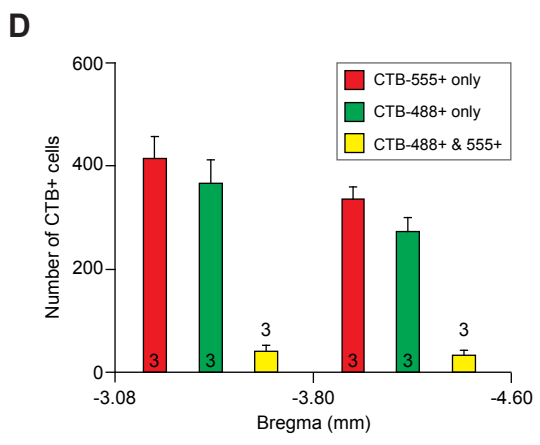
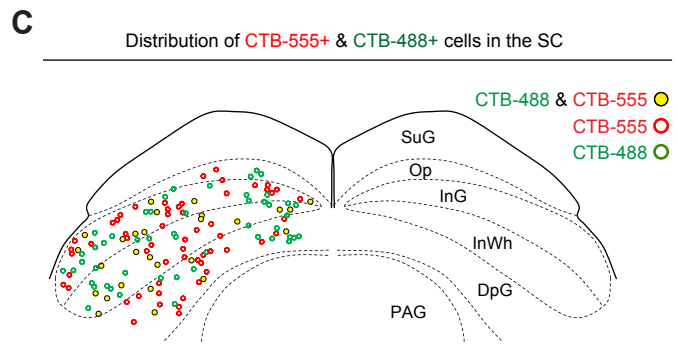
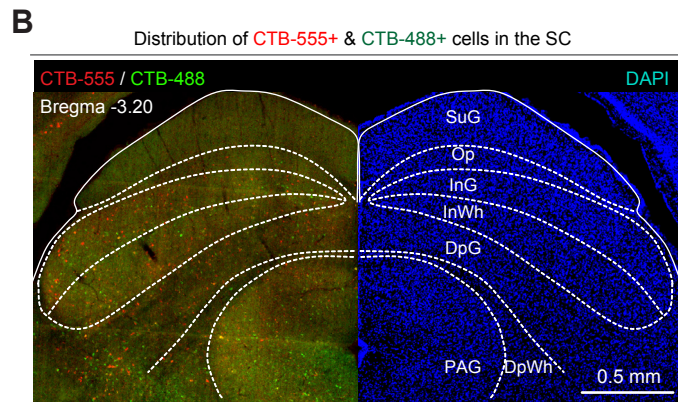
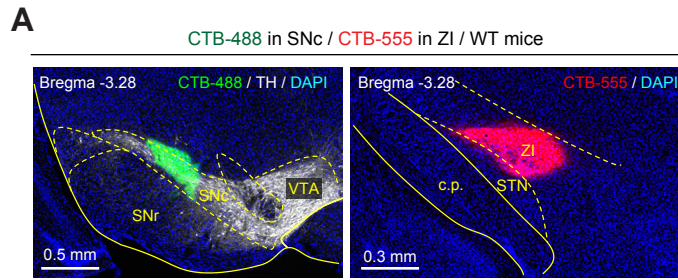


Figure S3 Huang et al., 2020

24 **Figure S3 SC-SNc pathway and SC-ZI pathway are anatomically segregated.**

25 (Related to Figure 1)

26 **(A)** Example coronal brain section showing injection of CTB-488 and CTB-555 into the
27 SNc (*left*) and ZI (*right*), respectively. The boundary of SNc was delineated according to
28 the immunofluorescence of TH (*left*). **(B, C)** An example coronal brain section (B) and the
29 corresponding illustration (C) showing the distribution of CTB-555+ & CTB-488+ cells in
30 the SC. **(D)** Quantitative analyses showing CTB-555+ & CTB-488+ cells in the SC were
31 largely segregated. Numbers of mice (D) are indicated in the graphs. Data in (D) are
32 means \pm SEM. Scale bars are labeled in the graphs.

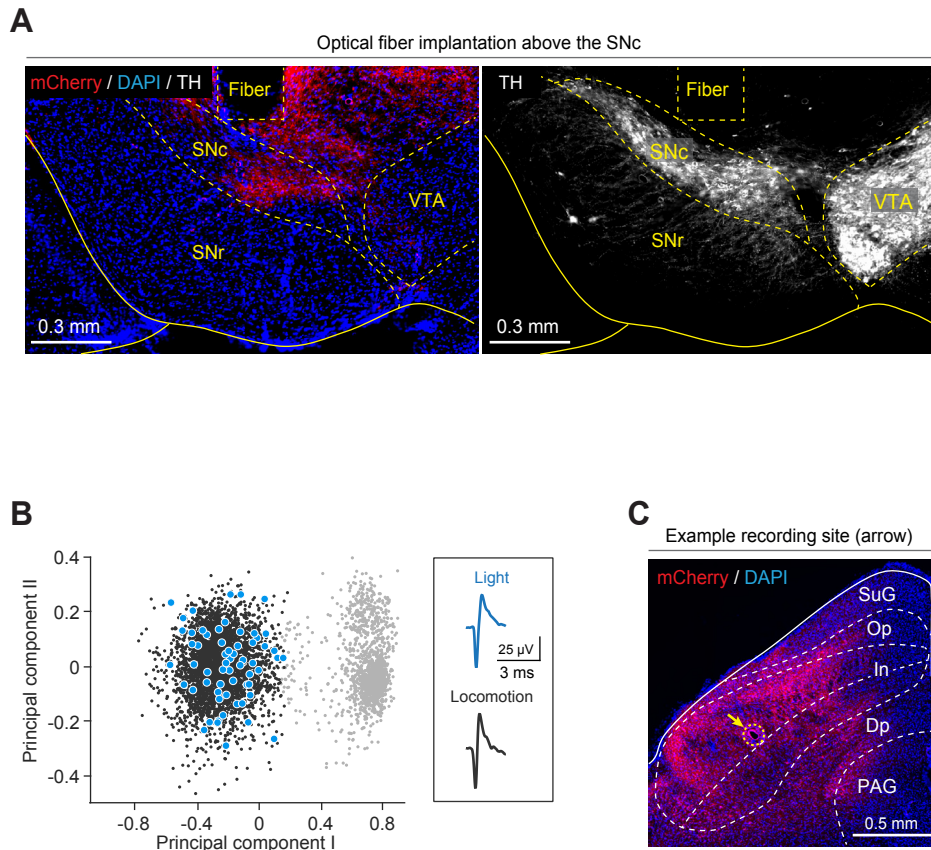


Figure S4 Huang et al., 2020

33 **Figure S4 SNc-projecting SC neurons encode the speed of locomotion.** (Related to
34 Figure 2)

35 **(A)** Example coronal section of the ventral midbrain showing the optical-fiber track above
36 ChR2-mCherry⁺ axon terminals in the SNc (*left*), the boundary of which was determined
37 by immunofluorescence of TH for dopamine neurons (*right*). **(B)** Principal component
38 analyses of light-evoked spikes (blue) and locomotion-evoked spikes (black) of an
39 example putative SNc-projecting SC neuron. Gray dots, noise. **(C)** Example coronal
40 section of the SC showing a recording site marked by electrolytic lesion (arrow) in the
41 intermediate layer (In) of the SC. Scale bars are labeled in the graphs.

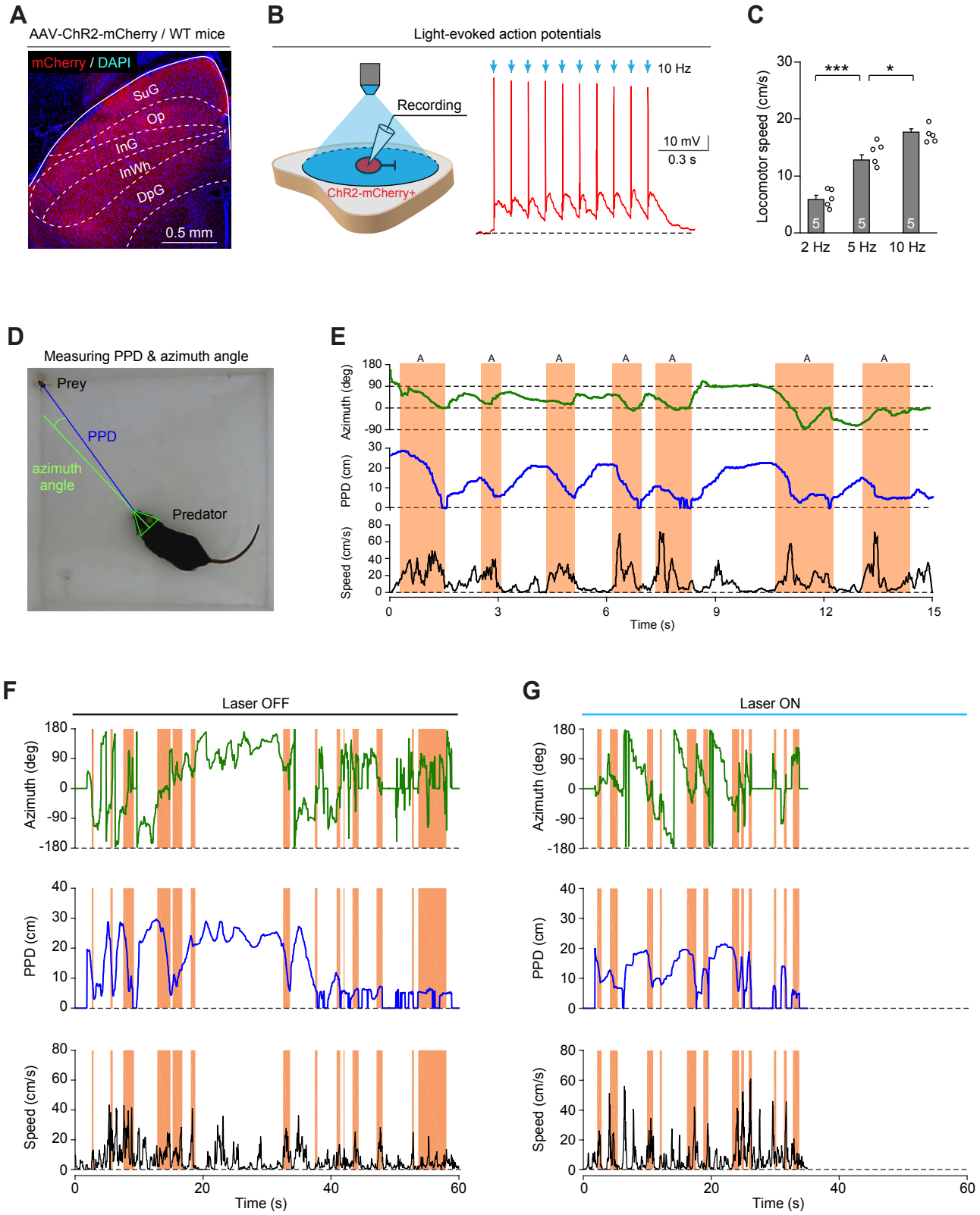


Figure S5 Huang et al., 2020

42 **Figure S5 Activation of the SC-SNc pathway promotes appetitive locomotion**
43 **during predatory hunting.** (Related to Figure 3)

44 **(A)** Example coronal section of the SC showing ChR2-mCherry expression in the SC of
45 WT mice. **(B)** Schematic diagram (*left*) and example trace (*right*) showing light pulses (2
46 ms, 473 nm, 10 Hz, 10 pulses) reliably triggered action potential firing from
47 ChR2-mCherry⁺ SC neurons in acute SC slices. **(C)** Quantitative analyses of average
48 locomotion speed of mice in the linear runway during photostimulation of the SC-SNc
49 pathway (10 ms, 6 s, 10 mW) with different frequencies (2 Hz, 5 Hz, 10 Hz). **(D)** An
50 example picture showing computer-aided measurement of azimuth angle and
51 prey-predator distance (PPD) when predator approached prey. **(E)** Aligned time courses
52 of azimuth angle (*top*), prey-predator distance (PPD, *middle*), and locomotion speed
53 (*bottom*) of an example mouse in predatory hunting, showing the identification of
54 approach episodes (shaded areas in orange). The intermittent approach episodes were
55 characterized by azimuth within a narrow range (-90 – 90 deg), by decreased PPD and
56 by pulses of locomotion speed. For the detailed criteria to identify the approach episodes,
57 see Methods. **(F, G)** Time courses of azimuth angle (*top*), PPD (*middle*), and locomotion
58 speed (*bottom*) during predatory hunting of an example mouse without (F, Laser OFF)
59 and with (G, Laser ON) photostimulation of the SC-SNc pathway. Numbers of mice (C)
60 are indicated in the graphs. Data in (C) are means \pm SEM. Statistic analyses (C) were
61 performed using Student t-test (*** P<0.001; * P<0.05). For the P values, see Table S4.
62 Scale bars are labeled in the graphs.

A

Ventral midbrain / AAV2-retro-mCherry-IRES-Cre / WT mice

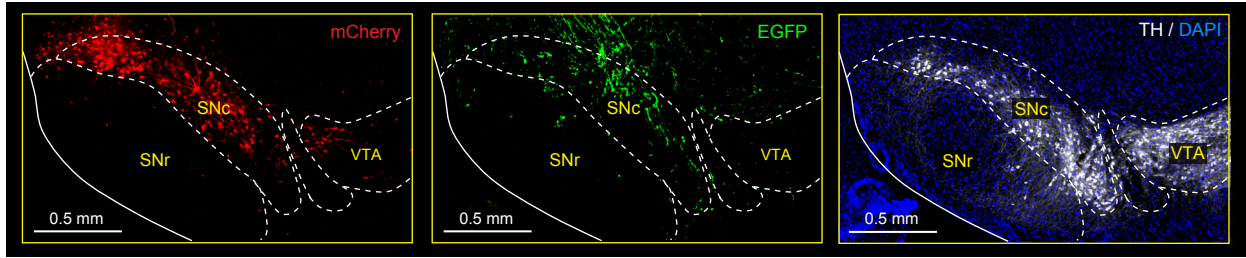
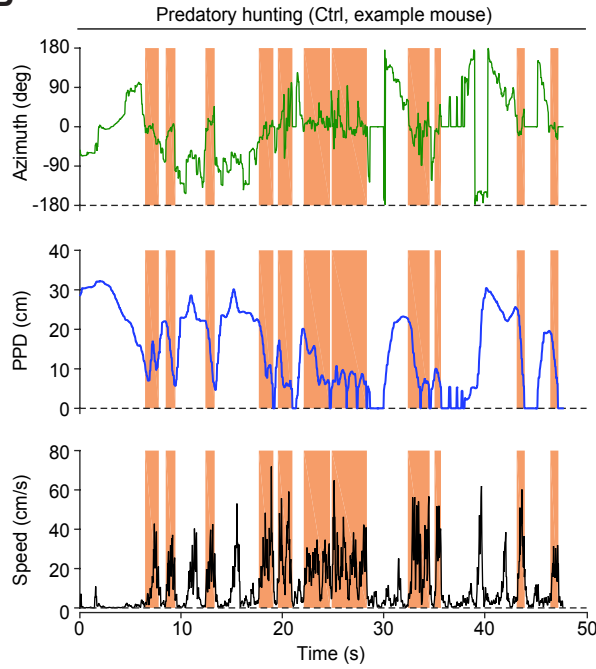
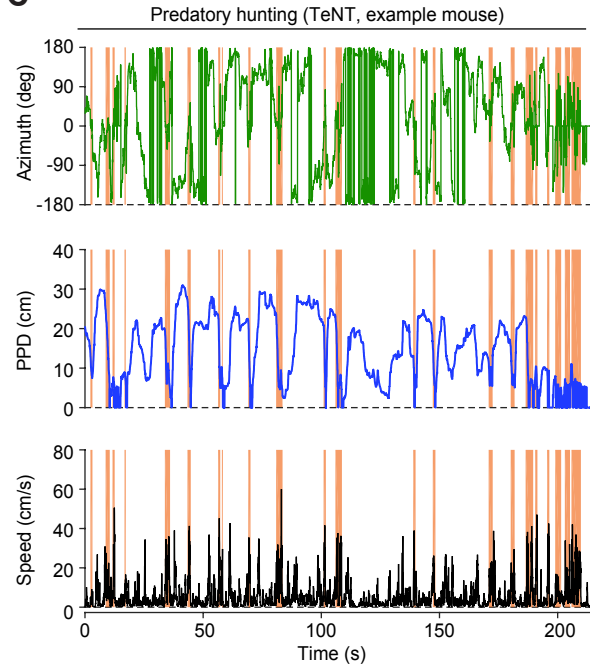
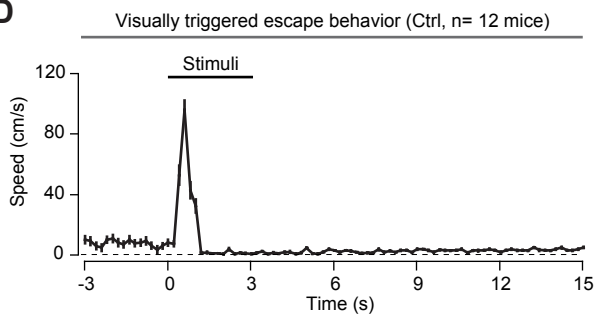
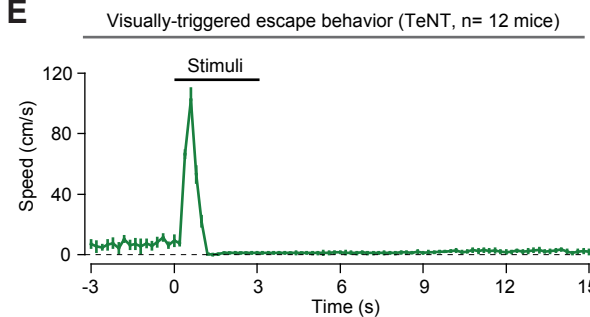
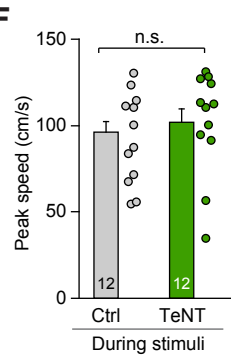
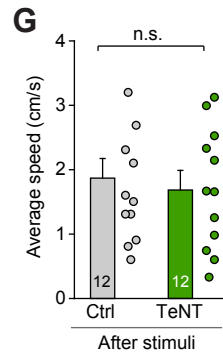
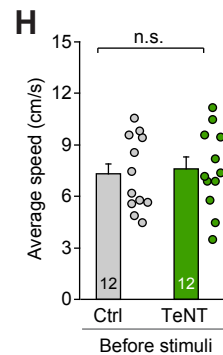
**B****C****D****E****F****G****H**

Figure S6 Huang et al., 2020

63 **Figure S6 The SNc-projecting SC neurons are required for appetitive locomotion**
64 **during predatory hunting.** (Related to Figure 4)

65 **(A)** Example coronal section of ventral midbrain showing mCherry+ cells in the SNc (*left*)
66 are intermingled with EGFP+ axon terminals from SC neurons (*middle*). The boundary of
67 the SNc is determined by immunofluorescence of TH (*right*). **(B, C)** Time courses of
68 azimuth angle (*top*), PPD (*middle*), and locomotion speed (*bottom*) during predatory
69 hunting of example mice without (B, Ctrl) and with (C, TeNT) synaptic inactivation of the
70 SNc-projecting SC neurons. **(D, E)** Time courses of locomotion speed before, during and
71 after looming visual stimuli in mice without (Ctrl, D) and with (TeNT, E) synaptic
72 inactivation of SNc-projecting SC neurons. **(F-H)** Quantitative analyses of peak
73 locomotion speed during stimuli (F), average locomotion speed after stimuli (G), and
74 average locomotion speed before stimuli (H) of mice without (Ctrl) and with (TeNT)
75 synaptic inactivation of SNc-projecting SC neurons. Scale bars are labeled in the graphs
76 (A). Numbers of mice are indicated in the graphs (D-H). Data in (D-H) are means \pm SEM.
77 Statistic analyses (F-H) are performed using Student t-test (n.s. $P > 0.1$). For the P values,
78 see Table S4.

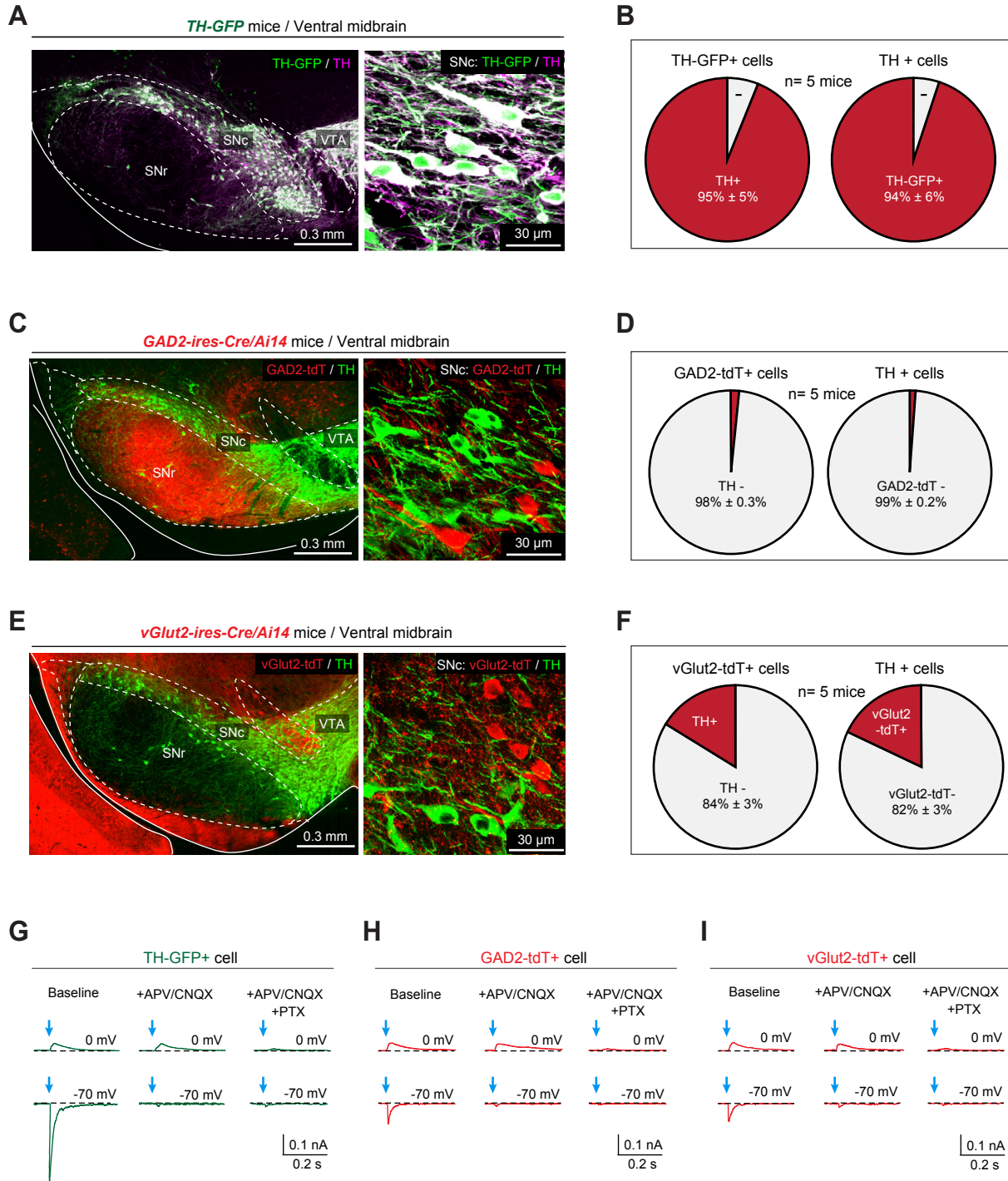


Figure S7 Huang et al., 2020

79 **Figure S7 Dopamine neurons are the primary postsynaptic target of the SC-SNc**
80 **pathway.** (Related to Figure 5)

81 **(A, B)** Example micrographs (A) and quantitative analyses (B) showing that TH-GFP+
82 cells and TH+ cells are largely overlapped in the SNc of *TH-GFP* mice. **(C, D)** Example
83 micrographs (C) and quantitative analyses (D) showing that GAD2-tdT+ cells and TH+
84 cells are largely segregated in the SNc of *GAD2-IRES-Cre/Ai14* mice. **(E, F)** Example
85 micrographs (E) and quantitative analyses (F) showing that vGlut2-tdT+ cells and TH+
86 cells are largely segregated in the SNc of *vGlut2-IRES-Cre/Ai14* mice. **(G-I)** Example
87 traces of oIPSCs (*top*) and oEPSCs (*bottom*) from putative SNc dopamine neurons
88 (TH-GFP+) (G), putative GAD2+ neurons (GAD2-tdT+) (H) and putative vGlut2+ neurons
89 (vGlut2-tdT+) (I) with and without perfusion of antagonists of glutamate receptors
90 (APV/CNQX) and GABA_A receptor (PTX). Numbers of mice (B, D, F) are indicated in the
91 graphs. Data in (B, D, F) are means \pm SEM. Scale bars are labeled in the graphs.

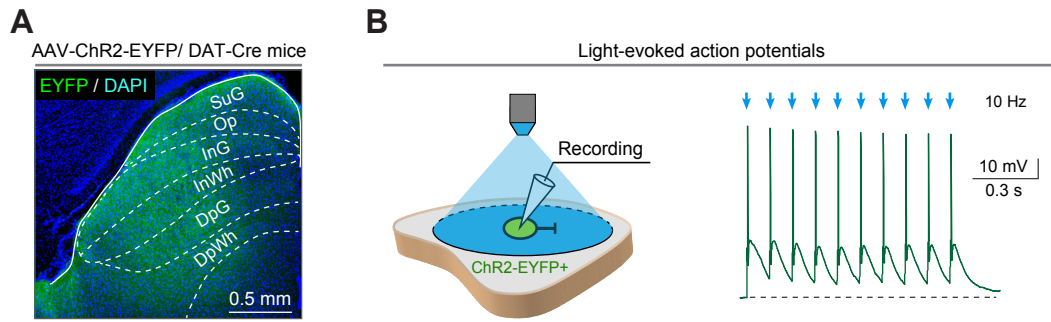


Figure S8 Huang et al., 2020

92 **Figure S8 SNc dopamine neurons mediate the effect of SC-SNc pathway activation.**

93 (Related to Figure 7)

94 **(A)** Example coronal section showing ChR2-EYFP expression in the SC. **(B)** Schematic
95 diagram (*left*) and example trace (*right*) showing light pulses (2 ms, 473 nm, 10 Hz, 10
96 pulses) reliably triggered action potential firing from ChR2-EYFP+ SC neurons in acute
97 SC slices. Scale bars are labeled in the graphs.

98 **Movie S1 Action potential firing of SNc-projecting SC neurons during locomotion**

99 This movie shows that the action potential firing of a putative SNc-projecting SC
100 neuron recorded with an optrode is correlated with locomotion. The action potentials
101 have been sorted and their waveforms are displayed in the corner of the movie.

102 **Movie S2 Predatory hunting of an example control mouse without**
103 **photostimulation of the SC-SNc pathway**

104 This movie shows behavioral analyses of predatory hunting of an example control
105 mouse without photostimulation of the SC-SNc pathway. The left part of the screen
106 displays the video taken by the overhead camera in parallel with computer-aided
107 analyses of azimuth angle and PPD in real-time. The right part of the screen displays the
108 time courses of azimuth angle, locomotion speed and PPD during predatory hunting in
109 real-time. The approach episodes were labeled with shaded areas in orange.

110 **Movie S3 Predatory hunting of an example test mouse with photostimulation of**
111 **the SC-SNc pathway**

112 This movie shows behavioral analyses of predatory hunting of an example test
113 mouse with photostimulation of the SC-SNc pathway. The left part of the screen displays
114 the video taken by the overhead camera in parallel with computer-aided analyses of
115 azimuth angle and PPD in real-time. The right part of the screen displays the time
116 courses of azimuth angle, PPD and locomotion speed during predatory hunting in
117 real-time. The approach episodes were labeled with shaded areas in orange.

118 **Movie S4 Predatory hunting of an example control mouse without synaptic**
119 **inactivation of SNc-projecting SC neurons**

120 This movie shows behavioral analyses of predatory hunting of an example control
121 mouse without synaptic inactivation of SNc-projecting SC neurons. The left part of the
122 screen displays the video taken by the overhead camera in parallel with computer-aided

123 analyses of azimuth angle and PPD in real-time. The right part of the screen displays the
124 time courses of azimuth angle, locomotion speed and PPD during predatory hunting in
125 real-time. The approach episodes were labeled with shaded areas in orange.

126 **Movie S5 Predatory hunting of an example test mouse with synaptic inactivation**
127 **of SNc-projecting SC neurons**

128 This movie shows behavioral analyses of predatory hunting of an example test
129 mouse with synaptic inactivation of SNc-projecting SC neurons. The left part of the
130 screen displays the video taken by the overhead camera in parallel with computer-aided
131 analyses of azimuth angle and PPD in real-time. The right part of the screen displays the
132 time courses of azimuth angle, locomotion speed and PPD during predatory hunting in
133 real-time. The approach episodes were labeled with shaded areas in orange.

134 **Movie S6 Defensive locomotion of an example control mouse without synaptic**
135 **inactivation of SNc-projecting SC neurons**

136 This movie shows the overhead looming visual stimuli triggered escape followed by
137 long-lasting freezing in an example control mouse without synaptic inactivation of
138 SNc-projecting SC neurons.

139 **Movie S7 Defensive locomotion of an example test mouse with synaptic**
140 **inactivation of SNc-projecting SC neurons**

141 This movie shows the overhead looming visual stimuli evoked immediate escape
142 followed by long-lasting freezing in an example test mouse with synaptic inactivation of
143 SNc-projecting SC neurons.

- 144 **Table S1 Mouse lines and reagents**
- 145 **Table S2 Summary of all experimental designs**
- 146 **Table S3 Summary of cell counting strategy**
- 147 **Table S4 Summary of statistical analyses**

Table S1 Mouse lines and reagents

Mouse Lines		
<i>vGlut2-IRES-Cre</i>	JAX Mice	Stock No: 016963
<i>GAD2-IRES-Cre</i>	JAX Mice	Stock No: 010802
<i>DAT-IRES-Cre</i>	JAX Mice	Stock No: 006660
<i>Ai14</i>	JAX Mice	Stock No: 007914
<i>TH-GFP</i>	Hideyuki Okano Lab	N/A
Antibodies		
Anti-EGFP	Abcam	ab290 / ab13970
Anti-mCherry	Abcam	ab167453 / ab205402
Anti-Glutamate	Sigma	G6642
Anti-GABA	Sigma	A2052
Anti-TH	Chemicon	AB152
Chemicals and tracers		
D-AP5 / CNQX / Picrotoxin	Tocris	Cat. No. 0106 / 0190 / 1128
TTX	Tocris	Cat. No. 1078
4-AP	Tocris	Cat. No. 0940
CTB-555 / 488	Thermofisher Scientific	Cat. No. C22843 / 22841
Clozapine N-oxide (CNO)	Enzo life sciences	Cat. No. BML-NS105-0025
Haloperidol	Sigma	Cat. No. H1512
AAV vectors		
AAV-DJ-hSyn-GRAB-DA	Shanghai Taitool Bioscience	N/A
AAV-DJ-hSyn-C1V1-mCherry	Shanghai Taitool Bioscience	N/A
AAV-DJ-hSyn-DIO-EGFP-2A-TeNT	Shanghai Taitool Bioscience	N/A
AAV-DJ-hSyn-DIO-hM4D-mCherry	Brain VTA Inc.	N/A
AAV-DJ-hSyn-ChR2-mCherry	Brain VTA Inc.	N/A
AAV-DJ-hSyn-mCherry	Brain VTA Inc.	N/A
AAV-DJ-hSyn-ChR2-EYFP	Brain VTA Inc.	N/A
AAV-DJ-hSyn-DIO-EGFP-Syb2	Brain VTA Inc.	N/A
AAV-DJ-hSyn-EGFP	Brain VTA Inc.	N/A
AAV-DJ-hSyn-DIO-EGFP	Brain VTA Inc.	N/A
AAV2-retro-hSyn-mCherry-ires-Cre	Brain VTA Inc.	N/A

Table S2 Summary of all experimental designs

Figures	Aims	Mouse lines	AAV injection & optical fiber implantation	Type of data
Figure 1 Figure S1	Cell-type-specific mapping of SC-SNc pathway	<i>vGlut2-ires-Cre</i> <i>GAD2-ires-Cre</i> <i>WT</i>	<i>AAV-hSyn-DIO-EGFP-Syb2</i> injected into the SC <i>CTB-555</i> injected into the SNc of WT mice	Histology
Figure S2	Segregation of SC-SNc and SC-VTA pathways	<i>WT</i>	<i>CTB-555 / CTB488</i> injected into the SNc and VTA, respectively <i>CTB-555 / CTB488</i> mixture injected into the SNc	Histology
Figure S3	Segregation of SC-SNc and SC-ZI pathways	<i>WT</i>	<i>CTB-555 / CTB488</i> injected into the SNc and ZI, respectively	Histology
Figure 2 Figure S4	SNc-projecting SC neurons encode locomotion speed	<i>WT</i>	<i>AAV-hSyn-ChR2-mCherry</i> injected into the SC Optical fibers implanted above the SNc	Single-unit recording
Figure 3 Figure S5	Activation of the SC-SNc pathway promotes appetitive locomotion	<i>WT</i>	<i>AAV-hSyn-ChR2-mCherry</i> injected into the SC Optical fibers implanted above the SNc	Behavior Histology Slice physiology
Figure 4 Figure S6	The SC-SNc pathway is selectively required for appetitive locomotion	<i>WT</i>	<i>AAV2-retro-mCherry-IRES-Cre</i> injected into the SNc <i>AAV-hSyn-DIO-EGFP-2A-TeNT</i> injected into the SC <i>AAV-hSyn-DIO-EGFP</i> (Ctrl) injected into the SC	Behavior Histology
Figure 5 Figure S7	Genetic labeling of different cell types in the SNc Synaptic innervation on SNc dopamine and non-dopamine neurons	<i>vGlut2-IRES-Cre</i> <i>GAD2-IRES-Cre</i> <i>Ai14</i> <i>TH-GFP</i>	<i>AAV-hSyn-ChR2-mCherry</i> injected into the SC	Histology Slice physiology
Figure 6	Activation of the SC-SNc pathway trigger dopamine release in the dorsal striatum	<i>WT</i>	<i>AAV-hSyn-C1V1-mCherry</i> injected into the SC <i>AAV-hSyn-GRAB-DA</i> injected into the dorsal striatum Optical fibers implanted above the SNc and dorsal striatum	Fiber photometry Histology Slice physiology
Figure 7 Figure S8	SNc dopamine neurons mediates the effect of the SC-SNc pathway activation	<i>DAT-IRES-Cre</i>	<i>AAV-hSyn-ChR2-EYFP</i> injected into the SC <i>AAV-hSyn-DIO-hM4D-mCherry</i> injected into the SNc <i>AAV-hSyn-DIO-mCherry</i> (Ctrl) injected into the SNc Optical fibers implanted above the SNc	Behavior Histology Slice physiology

Table S3 Summary of Cell Counting Strategy

Brain region	Superior Colliculus	SNc & VTA
Section type	Coronal section (40 μ m)	Coronal section (40 μ m)
Section Range	Bregma (-3.28 to -4.48)	Bregma (-2.80 to -3.80)
Total collection	Approximately 30 sections	Approximately 25 sections
Sampling	To sample 1 section every 5 sections to get 6 sections evenly spaced by 200 μ m	To sample 1 section every 5 sections to get 5 sections evenly spaced by 200 μ m

Table S4-1 Summary of statistical analyses

Figure	Sample size (n)	Statistical test	P values
1E	vGlut2-IRES-Cre = 5 mice GAD2-IRES-Cre = 5 mice	One-Way ANOVA	vGlut2-IRES-Cre vs. GAD2-IRES-Cre: P= 5.79939E-6 ***
3E	Laser OFF Ctrl = 5 mice ChR2 = 5 mice	Student t-test	ChR2 vs. Ctrl: P= 0.92794 n.s.
	Laser ON Ctrl = 5 mice ChR2 = 5 mice	Student t-test	ChR2 vs. Ctrl: P= 1.1324E-7 ***
	Laser OFF Ctrl = 5 mice ChR2 = 5 mice	Student t-test	ChR2 vs. Ctrl: P= 9.12091E-4 ***
3I	OFF = 12 mice ON = 12 mice	Student t-test	ON vs. OFF: P= 6.82E-09 ***
3J	OFF = 12 mice ON = 12 mice	Student t-test	ON vs. OFF: P= 7.61E-06 ***
3K	OFF = 12 mice ON = 12 mice	Student t-test	ON vs. OFF: P= 3.05E-06 ***
3L	OFF = 12 mice ON = 12 mice	Student t-test	ON vs. OFF: P= 0.15109 n.s.
3M	OFF = 12 mice ON = 12 mice	Student t-test	ON vs. OFF: P= 0.05989 n.s.
4E	Ctrl = 12 mice TeNT = 12 mice	Student t-test	TeNT vs. Ctrl: P= 0.0318 *
4F	Ctrl = 12 mice TeNT = 12 mice	Student t-test	TeNT vs. Ctrl: P= 0.41367 n.s.
4G	Ctrl = 12 mice TeNT = 12 mice	Student t-test	TeNT vs. Ctrl: P= 0.66311 n.s.
4H	Ctrl = 12 mice TeNT = 12 mice	Student t-test	TeNT vs. Ctrl: P= 0.00107 **
4I	Ctrl = 12 mice TeNT = 12 mice	Student t-test	TeNT vs. Ctrl: P= 0.00105 **
5E	TH-GFP+ cells = 10 cells GAD2-tdT+ cells = 10 cells	Student t-test	TH-GFP+ oEPSC vs. oIPSC: P= 7.93268E-7 ***
			GAD2-tdT+ oEPSC vs. EGFP+ oIPSC: P= 5.01684E-4 *** oEPSC TH-GFP+ vs. GAD2-tdT+: P= 1.22279E-5 ***
5G	TH-GFP+ cells = 11 cells GAD2-tdT+ cells = 10 cells	Student t-test	TH-GFP+ oEPSC vs. oIPSC: P= 2.13383E-7 ***
			GAD2-tdT+ oEPSC vs. oIPSC: P= 3.09254E-6 *** oEPSC TH-GFP+ vs. GAD2-tdT+: P= 1.11192E-5 ***
6H	GRAB-DA = 6 mice EGFP = 6 mice	One-Way ANOVA	GRAB-DA vs. EGFP: P= 6.152478E-18 ***
6J	Saline = 6 mice Haldol 0.4 mg/kg = 6 mice Haldol 1.6 mg/kg = 6 mice	One-Way ANOVA	Saline vs. Haldol 0.4 mg/kg: P= 4.22687E-7 ***
			Saline vs. Haldol 1.6 mg/kg: P= 7.35846E-12 ***

Table S4-2 Summary of statistical analyses

Figure	Sample size (n)	Statistical test	P values
7D	Before CNO = 7 cells After CNO = 7 cells	Student t-test	After CNO vs. Before CNO: P= 2.41E-05 ***
7E	Saline-OFF = 8 mice Saline-ON = 8 mice	Student t-test	Saline - OFF vs. ON: P= 8.63528E-6 ***
	CNO-OFF = 8 mice CNO-ON = 8 mice	Student t-test	CNO - OFF vs. ON: P= 4.79306E-4 ***
7F	Saline = 8 mice CNO = 8 mice	Student t-test	CNO vs. Saline: P= 5.90024E-07 ****
7G	Saline-OFF = 8 mice Saline-ON = 8 mice	Student t-test	Saline - OFF vs. ON: P= 1.18523E-5 ***
	CNO-OFF = 8 mice CNO-ON = 8 mice	Student t-test	CNO - OFF vs. ON: P= 0.01231 *
7H	Saline = 8 mice CNO = 8 mice	Student t-test	CNO vs. Saline: P= 7.82681E-6 ***
S5C	2 Hz = 5 mice	Student t-test	5 Hz vs. 2 Hz: P= 1.25213E-4 ***
	5 Hz = 5 mice	Student t-test	10 Hz vs. 5 Hz: P= 0.0204 *
	10 Hz = 5 mice		
S6F	Ctrl = 12 mice TeNT = 12 mice	Student t-test	TeNT vs. Ctrl: P= 0.41367 n.s.
S6G	Ctrl = 12 mice TeNT = 12 mice	Student t-test	TeNT vs. Ctrl: P= 0.66311 n.s.
S6H	Ctrl = 12 mice TeNT = 12 mice	Student t-test	TeNT vs. Ctrl: P= 0.79514 n.s.